

# Rapidly growing black holes and host galaxies in the distant Universe from the *Herschel* Radio Galaxy Evolution Project <sup>★</sup>

G. Drouart<sup>1,2,3,4</sup>, C. De Breuck<sup>1</sup>, J. Vernet<sup>1</sup>, N. Seymour<sup>3</sup>, M. Lehnert<sup>2</sup>, P. Barthel<sup>5</sup>, F. E. Bauer<sup>6,7</sup>, E. Ibar<sup>6,8</sup>, A. Galametz<sup>9</sup>, M. Haas<sup>10</sup>, N. Hatch<sup>11</sup>, J. R. Mullaney<sup>12</sup>, N. Nesvadba<sup>13</sup>, B. Rocca-Volmerange<sup>2</sup>, H. J. A. Röttgering<sup>14</sup>, D. Stern<sup>15</sup>, D. Wylezalek<sup>1</sup>

<sup>1</sup>European Southern Observatory, Karl Schwarzschild Straße 2, 85748 Garching bei München, Germany

<sup>2</sup>Institut d'Astrophysique de Paris, 98bis boulevard Arago, 75014 Paris, France

<sup>3</sup>CSIRO Astronomy & Space Science, PO Box 76, Epping, NSW 1710, Australia

<sup>4</sup>Department of Earth and Space Science, Chalmers University of Technology, Onsala Space Observatory, 43992 Onsala, Sweden

<sup>5</sup>Kapteyn Astronomical Institute, Univ. of Groningen, Netherlands

<sup>6</sup>Instituto de Astrofísica, Facultad de Física, Pontificia Universidad Católica de Chile, 306, Santiago 22, Chile

<sup>7</sup>Space Science Institute, 4750 Walnut Street, Suite 205, Boulder, Colorado 80301

<sup>8</sup>Instituto de Física y Astronomía, Universidad de Valparaíso, Avda. Gran Bretaña 1111, Valparaíso, Chile

<sup>9</sup>INAF - Osservatorio di Roma, Via Frascati 33, I-00040, Monteporzio, Italy

<sup>10</sup>Astronomisches Institut, Ruhr-Universität Bochum, Universitätsstr. 150, 44801 Bochum, Germany

<sup>11</sup>School of Physics and Astronomy, University of Nottingham, University Park, Nottingham, NG7 2RD, UK

<sup>12</sup>Department of Physics, Durham University, South Road, Durham, DH1 3LE, UK

<sup>13</sup>Institut d'Astrophysique Spatiale, CNRS, Université Paris-Sud, 91405, Orsay, France

<sup>14</sup>Leiden Observatory, University of Leiden, P.O. Box 9513, 2300 RA Leiden, Netherlands

<sup>15</sup>Jet Propulsion Laboratory, California Institute of Technology, Mail Stop 169-221, Pasadena, CA 91109, USA

accepted for publication, A&A, 28 March 2014

## ABSTRACT

We present results from a comprehensive survey of 70 radio galaxies at redshifts  $1 < z < 5.2$  using the PACS and SPIRE instruments on-board the *Herschel Space Observatory*. Combined with existing mid-IR photometry from the *Spitzer Space Telescope*, published  $870 \mu\text{m}$  photometry and new observations obtained with LABOCA on the APEX telescope, the spectral energy distributions (SEDs) of galaxies in our sample are continuously covered across  $3.6\text{--}870 \mu\text{m}$ . The total  $8\text{--}1000 \mu\text{m}$  restframe infrared luminosities of these radio galaxies are such that they almost all are either ultra- $(L_{\text{tot}}^{\text{IR}} > 10^{12} L_{\odot})$  or hyper-luminous  $(L_{\text{tot}}^{\text{IR}} > 10^{13} L_{\odot})$  infrared galaxies. We fit the infrared SEDs with a set of empirical templates which represent dust heated (1) by a variety of starbursts (SB) and (2) by an active galactic nucleus (AGN). We find that the SEDs of radio galaxies require the dust to be heated by both AGN and SB, but the luminosities of these two components are not strongly correlated. Assuming empirical relations and simple physical assumptions, we calculate the star formation rate (SFR), the black hole mass accretion rate ( $\dot{M}_{\text{BH}}$ ), and the black hole mass ( $M_{\text{BH}}$ ) for each radio galaxy. We find that the host galaxies and their black holes are growing extremely rapidly, having  $\text{SFR} \approx 100\text{--}5000 M_{\odot} \text{yr}^{-1}$  and  $\dot{M}_{\text{BH}} \approx 1\text{--}100 M_{\odot} \text{yr}^{-1}$ . The mean specific star formation rates (sSFR) of radio galaxies at  $z \gtrsim 2.5$  are higher than the sSFR of typical star-forming galaxies over the same redshift range but are similar or perhaps lower than the galaxy population for radio galaxies at  $z \lesssim 2.5$ . By comparing the sSFR and the specific black hole mass accretion rate, we conclude that black holes in radio loud AGN are already, or soon will be, overly massive compared to their host galaxies in terms of expectations from the local  $M_{\text{BH}}\text{--}M_{\text{Gal}}$  relation. In order to “catch up” with the black hole, the galaxies require about an order-of-magnitude more time to grow in mass, at the observed SFRs, compared to the time the black hole is actively accreting. However, during the current cycle of activity, we argue that this catching-up is likely to be difficult due to the short gas depletion times. Finally, we speculate on how the host galaxies might grow sufficiently in stellar mass to ultimately fall onto the local  $M_{\text{BH}}\text{--}M_{\text{Gal}}$  relation.

**Key words.** Galaxies: high redshift – Galaxies: active – Infrared: galaxies

## 1. Introduction

At high redshifts, deep sub-mm observations suggest that massive galaxies have high flux densities and vigorous, on-going star formation (e.g. Hughes et al., 1998; Barger et al., 1998; Stevens et al., 2003; Chapman et al., 2005; Wardlow et al., 2011; Swinbank et al., 2013). The sensitivity of wide-field bolometer arrays limits these studies to only the brightest sub-mm emitters (e.g. Weiß et al., 2009). Such bright sub-mm galaxies (SMGs)

frequently appear to be highly disturbed, which favours gas inflows driven by mergers as the chief instigator for generating the high observed sub-mm fluxes (e.g. Somerville et al., 2001; Engel et al., 2010). Whether these intense starbursts are indeed driven by mergers or by high rates of cold gas accretion is a question that is still actively debated (e.g. Noeske et al., 2007; Daddi et al., 2007; Tacconi et al., 2008).

Often, vigorous star formation is accompanied by powerful active galactic nuclei (AGN; e.g. Hopkins & Quataert, 2010; Wang et al., 2011; Seymour et al., 2012; Rosario et al., 2012). The presence of AGN is revealed throughout the electromagnetic spectrum, from X-rays to radio, and in both continuum and

<sup>★</sup> *Herschel* is an ESA space observatory with science instruments provided by European-led Principal Investigator consortia and with important participation from NASA.

line emission (e.g. Carilli et al., 1997; Hardcastle & Worrall, 1999; Vernet et al., 2001; Alexander et al., 2005; Ogle et al., 2006; Nesvadba et al., 2008; Ivison et al., 2012; Wang et al., 2013). How AGN are triggered remains one of the most challenging questions of contemporary extragalactic astrophysics (see Alexander & Hickox, 2012, for a recent review). Even if current solutions and simulations are not completely satisfying (e.g. Hopkins & Quataert, 2010), it is evident that the same material, cold molecular gas, is the reservoir out of which stars are formed and the AGN is fuelled (e.g. Hicks et al., 2009).

Interestingly, the expected correlation between AGN activity and star-formation rate is not obvious in observations, both locally and at high redshift (e.g. Netzer, 2009; Hatziminaoglou et al., 2010; Asmus et al., 2011; Dicken et al., 2012; Bongiorno et al., 2012; Harrison et al., 2012; Rosario et al., 2012, 2013; Feltre et al., 2013; Videla et al., 2013; Esquej et al., 2014; Leipski et al., 2014). This may be due to high variability of AGN (Hickox et al., 2011) or the differences in timescales it takes for gas to become unstable, collapse to form stars over kpc scales compared to the time it takes for gas to lose sufficient angular momentum to reach the inner central parsec of the galaxy (Jogee et al., 2005). Despite our difficulties in understanding how relationships between the host galaxy and super massive black holes come about, we observe a tight correlation between the black hole and the physical properties of their host galaxies in the local universe (e.g. Magorrian et al., 1998; Gebhardt et al., 2000; Ferrarese & Merritt, 2000; Häring & Rix, 2004). These relations suggest that both components of galaxies grew simultaneously (e.g. Hopkins et al., 2006). Nevertheless, some discrepancies have been observed from the local relation implying either an observational bias or a possible evolution of this relation with redshift (e.g. Lauer et al., 2007; Zhang et al., 2012). Currently, there are no complete answers that reconcile all the observations (Kormendy & Ho, 2013, for a recent review).

Observations of infrared emission plays a key role in disentangling the relative importance of star formation and AGN to the bolometric emission from galaxies. As the IR emission is a mixture of dust heated by both the stars and the AGN, the nature of the IR spectral energy distribution (SED) can be used to probe the relative growth of galaxies and supermassive black holes and how their growth rates are related (the “AGN-starburst connection”). The short cooling time of the dust provides us with a snapshot of the heating rate of a galaxy due to the re-emission of absorbed UV and optical photons (e.g. Draine, 2003). However, the peak of the IR SED, where both heating of dust grains by AGN and star formation make important contributions, was not completely covered with good sensitivity by *Spitzer* or by ground-based sub-mm photometry for distant galaxies (e.g. Archibald et al., 2001; Reuland et al., 2004; Cleary et al., 2007; De Breuck et al., 2010; Rawlings et al., 2013). *Herschel* now provides the first opportunity to explore the complete IR SED of high redshift AGN, and thus to examine the relative contribution of the AGN and star formation to the bolometric luminosity of galaxies over a wide range of redshift.

Powerful radio galaxies are crucial objects in understanding the evolution of massive galaxies. They present all phenomenology undergoing both active star formation and rapidly accreting supermassive black holes. Powerful radio jets, strong and highly ionized optical and near-IR emission lines, and luminous mid-IR continuum, for example, betray the presence of an accreting supermassive black hole (e.g. Carilli et al., 1997; Vernet et al., 2001; Nesvadba et al., 2008; De Breuck et al., 2010; Drouart et al., 2012; Rawlings et al., 2013). They also have luminous submm emission, which is directly related to their vigorous star for-

mation. Moreover, they have elliptical light profiles (Matthews et al., 1964; van Breugel et al., 1998; Pentericci et al., 1999; Zirm et al., 2003), are extremely massive (Rocca-Volmerange et al., 2004; Seymour et al., 2007) and are often associated with high density environments (e.g. Venemans et al., 2007; Falder et al., 2010; Hatch et al., 2011; Kuiper et al., 2011; Galametz et al., 2012; Wylezalek et al., 2013a). In other words, they have many hallmarks of a massive (perhaps cluster) galaxy in formation (Miley & De Breuck, 2008).

By their fortuitous edge-on orientation, the radio galaxies present a dusty torus occulting the light from the hot accretion disk (type 2 AGN), enabling the simultaneous study of the host galaxy and the AGN, more easily than in the case of quasars (i.e. type 1 AGN, for a recent review, see Antonucci, 2011). Therefore, observing and characterising the different constituents of high redshift radio galaxies appears as our best chance to gain insights on the connection of the galaxy and black hole growth at much earlier stage in their history, more especially during the peak of the cosmic AGN and star formation activity (Hopkins & Beacom, 2006; Aird et al., 2010). Since characterising the host galaxy/BH through dynamic properties at high redshift is observationally expensive (Nesvadba et al., 2011), and beyond the reach of most of the current facilities, one has to rely on energetic diagnostics (such as SED decomposition) and empirical relations (Ferrarese & Merritt, 2000; Häring & Rix, 2004; Merloni et al., 2010, e.g.  $M_{\text{BH}}-\sigma$ ,  $M_{\text{BH}}-M_{\text{bulge}}$ ,  $M_{\text{BH}}-M_K$ ) to investigate this (non-)relation during the first half of the history of the Universe in larger samples.

In this paper, we analyse the characteristics of the IR SEDs of a sample of 70 powerful radio galaxies spanning the redshift range from 1 to 5.2. This large sample allows us to compare the properties of the IR SED with their other characteristics (e.g. radio luminosities and sizes). The paper is organised as follows: § 2 outlines the *Herschel* and sub-mm observations and data reduction; § 3 demonstrates how the photometry was calculated in cases of isolated and blended sources in the *Herschel* images; § 4 discusses the IR luminosities and the SED fitting procedure which was used to estimate the bolometric, AGN and starburst luminosities; § 5 compares the IR emission with other properties of the radio galaxies; § 6 discusses the interpretation of these luminosities in terms of physical parameters allowing us to put new constraints on the evolution of radio galaxies. Throughout this paper, we adopt the concordance cosmological model ( $H_0 = 70 \text{ km s}^{-1} \text{ Mpc}^{-1}$ ,  $\Omega_\Lambda = 0.7$ ,  $\Omega_M = 0.3$ ).

## 2. Observations and Data reduction

This paper aims to disentangle the IR SED of a sample of 70 powerful radio galaxies spanning the redshift range 1–5.2. This HeRGÉ Radio Galaxies Evolution (HeRGÉ) sample is identical to the *Spitzer* High- $z$  Radio Galaxies (SHzRG) sample described by Seymour et al. (2007) and De Breuck et al. (2010). We briefly summarize here the selection criteria to build this sample. The radio galaxies have been selected to cover homogeneously the radio luminosity-redshift plane, applying the criteria  $L^{3 \text{ GHz}} > 10^{26} \text{ W Hz}^{-1}$ , where  $L^{3 \text{ GHz}}$  is the total luminosity at a rest-frame frequency of 3 GHz (Table 1; Seymour et al., 2007).

We first describe the new *Herschel* data of our entire sample, followed by a presentation of sub-mm data which were obtained

with the LARge Bolometer CAmera (LABOCA) on the APEX telescope to complete the submm observations of our sample<sup>1</sup>.

### 2.1. Far-IR data, *Herschel*

The far-IR data for all 70 sources were obtained with the *Herschel Space Observatory* (Pilbratt et al., 2010) in five broad bands: in two bands with PACS (Photodetector Array Camera and Spectrometer; Poglitsch et al., 2010, at 160  $\mu\text{m}$  and either 70  $\mu\text{m}$  or 100  $\mu\text{m}$  depending on the redshift of the radio galaxy) and in three bands with SPIRE (Spectral and Photometric Imaging REceiver; Griffin et al., 2010, at 250, 350 and 500  $\mu\text{m}$ ). Our program was observed between 2011 February and 2012 March. Several sources were already observed as part of guaranteed time observations, and those data were obtained from the *Herschel* Science Archive (see Table 2 for program and ObsID).

#### 2.1.1. PACS reduction

PACS covers the spectral region 60 to 210  $\mu\text{m}$ . The “mini-scan map mode” was used on each science target, using the PACS (70  $\mu\text{m}$ )/PACS (160  $\mu\text{m}$ ) and PACS (100  $\mu\text{m}$ )/PACS (160  $\mu\text{m}$ ) configurations for sources at  $z < 2$  and  $z > 2$ , respectively. Each observation consisted of two cross-scan images centred on the source. The final map covers about 2x4 arcmin, with homogeneous coverage of 50 arcsec diameter around the target. The observations of PKS 1138-262 cover a larger field but were reduced using the same procedure. As each PACS observation consists of a simultaneous scan in two bands at medium scan speed (20 arcsec.s<sup>-1</sup>), two sub-images are produced for each band and co-added to obtain the final maps. Each data set was reduced from level 0 using the *Herschel* Interactive Processing Environment, version 8 (HIPE; Ott, 2010) using the standard *deep miniscan* pipeline. As we are looking for faint sources, the *MMTDeglitching* task was applied on level 0.5 of the data and we checked on the coverage map that no flux was potentially removed from the source. The PACS data is dominated by 1/f noise, so we applied a *high-pass filter* on level 1 data with a *high-pass filtering radius* (*hpfradius*) value of 15 readouts for the blue/green channel and 25 readouts for the red channel with a circular mask of 15 arcsec radius centred on the galaxy coordinates (best strategy available, see Popesso et al., 2012). Finally, each map was projected onto a user-defined world coordinate system (WCS) grid centred on the source. As our observations have a high redundancy, we chose a small *pixfraction* value (0.01) and set the *pixsize* to the recommended values: 2 arcsec for the blue/green channel and 3 arcsec for the red channel (Table 1)<sup>2</sup>. Finally, the 2 sub-maps were co-added into a final map with the *MosaicTask*.

#### 2.1.2. SPIRE reduction

SPIRE covers the spectral region 200 to 700  $\mu\text{m}$ . Each observation with SPIRE consists of three successive scans centred on

<sup>1</sup> For our sample of radio galaxies, synchrotron contamination at submm wavelength is negligible as all sources present steep radio spectral indices.

<sup>2</sup> We also test the reduction with smaller pixel size (1.2 and 2.1 arcsec for the blue/green and red channels) and find the differences on the final flux to be negligible (<5%). See also PACC-ME-TN-033 (April 4, 2012 v2) at [http://herschel.esac.esa.int/twiki/pub/Public/PacsCalibrationWeb/bolopsf\\_20.pdf](http://herschel.esac.esa.int/twiki/pub/Public/PacsCalibrationWeb/bolopsf_20.pdf) for further information on the pixelisation effect on the PSF.

the source with all three bands (250, 350 and 500  $\mu\text{m}$ ) at 30 arcsec.s<sup>-1</sup> scan speed. The only exception is again PKS 1138-262 which had four scans over a wider area. The final map for each source covers 8x10 arcmin, with a homogeneous exposure level throughout the entire field. We reduced the data with the *Photometer small map pipeline* within version 8 of HIPE. As glitches are present in the SPIRE timeline, several deglitching procedures were applied to the level 1 data. We choose the *linearadaptive20* option for the *wavelet deglitcher* with all the other options at their default values. We used the *naivemapmaker* to create the final map with pixel sizes of 6, 10, and 14 arcsec for the maps at 250, 350, and 500  $\mu\text{m}$  maps, respectively (Table 1).

### 2.2. *Herschel* Photometry

Thanks to high resolution radio observations (Carilli et al., 1997; Pentericci et al., 2000; De Breuck et al., 2010), radio galaxy positions are known to sub-arcsec accuracy. As the average *Herschel* pointing uncertainties are  $\sim 1$  arcsec, we performed fixed aperture photometry directly on the known position of the each radio galaxy. Due to the depth of the images and the large beam of *Herschel*, the aperture photometry is often contaminated by nearby companions, which may contribute significantly to the estimated flux of the radio galaxy. In order to mitigate against this contamination, we visually checked each galaxy in six bands, from MIPS (24  $\mu\text{m}$ ) to SPIRE (500  $\mu\text{m}$ ). As the 24  $\mu\text{m}$  image provides the best spatial resolution with which to investigate the dust emission, it was used to isolate potential companions contributing to the total flux in the *Herschel* data. The SPIRE (250  $\mu\text{m}$ ) image, since it is taken through one of the most sensitive channels and has reasonable resolution, was used to provide long wavelength information about possible contaminated sources. We first mark all the positions of detected sources in the 24  $\mu\text{m}$  image onto the *Herschel* maps. When a possible contaminating source was found within 60 arcsec, it was deblended to remove its contribution from the radio galaxy flux (see § 2.2.2). Otherwise, a single aperture was used to estimate the flux (Table 3).

#### 2.2.1. Isolated sources

When the image does not show a contamination in the MIPS (24  $\mu\text{m}$ ) and SPIRE (250  $\mu\text{m}$ ) images, aperture photometry was performed using the *AnnularSkyAperturePhotometry* task within HIPE. For a comparison between the different strategies, we refer to Popesso et al. (2012); Pearson et al. (2013), for PACS and SPIRE, respectively. We summarise here briefly for our sample. For PACS, the optimal strategy of masking is applied (see § 2.1.1), and aperture and PSF photometry gives similar results. For SPIRE, as our sample contains mainly faint sources ( $F^{gal} < 30\text{mJy}$ ), automatic procedures would normally be preferred (SUSSEXtractor or DAophot). However, as our sample is subject to blending effects (see next section), PSF-photometry is mainly performed to measure source flux making use of Starfinder (similar to SUSSEXtractor). See Table 1 for a summary of the parameters. Table 3 reports the final flux, obtained after aperture correction in the case of aperture photometry.

#### 2.2.2. Blended sources

Blending becomes more important, particularly for the SPIRE bandpasses where the large beams encompass a large area around the radio galaxy (for example, the SPIRE 500  $\mu\text{m}$  beam

**Table 1.** Main parameters of the *Herschel* bands and photometry for isolated sources. The  $3\sigma$  sensitivity limit is the average sensitivity calculated over our entire sample for each band. Absolute calibration uncertainties and aperture correction from <http://herschel.esac.esa.int/Documentation.shtml>. Note that this correction is only applied for the aperture photometry (see § 2.2).

| Bands                      | beam size<br>[arcsec] | absolute cal. | final pixel size<br>[arcsec] | Av. $3\sigma$ sensitivity<br>[mJy] | aperture<br>[arcsec] | inner sky<br>[arcsec] | outer sky<br>[arcsec] | Ap. corr. |
|----------------------------|-----------------------|---------------|------------------------------|------------------------------------|----------------------|-----------------------|-----------------------|-----------|
| PACS (70 $\mu\text{m}$ )   | 5.6                   | 5%            | 2                            | 8.7                                | 7                    | 15                    | 25                    | 1.33      |
| PACS (100 $\mu\text{m}$ )  | 6.7                   | 5%            | 2                            | 10.8                               | 7                    | 15                    | 25                    | 1.39      |
| PACS (160 $\mu\text{m}$ )  | 11                    | 5%            | 3                            | 24.6                               | 11                   | 15                    | 30                    | 1.37      |
| SPIRE (250 $\mu\text{m}$ ) | 18                    | 7%            | 6                            | 15.9                               | 22                   | 60                    | 90                    | 1.28      |
| SPIRE (350 $\mu\text{m}$ ) | 25                    | 7%            | 10                           | 17.7                               | 30                   | 60                    | 90                    | 1.19      |
| SPIRE (500 $\mu\text{m}$ ) | 36                    | 7%            | 14                           | 18.9                               | 42                   | 60                    | 90                    | 1.26      |

corresponds to  $\sim 300$  kpc at  $z=1$ ). While this is particularly problematic for blind source extraction at a single wavelength (Nguyen et al., 2010), we can use here the prior information given by higher resolution observations such as MIPS (24  $\mu\text{m}$ ) images.

We use Starfinder, software optimised for crowded fields, performing Point Spread Function (PSF) photometry to estimate the fluxes of sources which are blended (Diolaiti et al., 2000). StarFinder requires both the estimated position of each source and the characteristics of the PSF. We defined a 2D Gaussian PSF with the FWHM equal to the beam size. Even if the PACS and SPIRE beams are slightly different from Gaussian, the energy in the secondary lobes is only a small fraction of the total integrated energy, and the Gaussian approximation is still valid. We checked this difference in the SPIRE images where several sources can be used to estimate the PSF. We found the differences to be negligible.

Even with input positions on possible sources, sometimes Starfinder did not converge on a solution, especially in the case where two sources are separated by less than the FWHM of the PSF for SPIRE. The SPIRE 500  $\mu\text{m}$  band, which has the largest beam, is the most affected by this effect. For sources that could not be accurately deblended, we assume the total flux to be the upper limit for the radio galaxy.

The main caveat to this technique is the assumption that a source detected in SPIRE has a counterpart in the MIPS images. Using the average sensitivity of our MIPS (24  $\mu\text{m}$ ) and SPIRE (250  $\mu\text{m}$ ) images, we calculate the corresponding colour limit,  $\log(F_{250\mu\text{m}}/F_{24\mu\text{m}})=2.12$ . Making use of templates from DecomPIR (see § 4), we indeed find that this approach can miss some sources at  $z>3$  given our achieved sensitivities. Nevertheless, such contamination is estimated to be only a few percent (Roseboom et al., 2010; Magdis et al., 2011) and is therefore not taken into account for the remainder of this paper.

### 2.2.3. Uncertainties

The design of the PACS detectors makes those data prone to correlated noise (Popesso et al., 2012). While a formal estimate of such noise is almost impossible, it is possible to estimate the average total noise from the images. Given the observing strategy, we focused on the most homogeneous, central part of the images to estimate the noise. We drew identical, non-overlapping apertures around the source in a hexagonal pattern, and performed the same aperture photometry as used to estimate the flux of the central source. We considered the total noise on the map to be the standard deviation of these distributed apertures around the source.

For the SPIRE images, the uncertainties are calculated either in the sky annulus for the aperture photometry in the case of an isolated source, or by the standard deviation of the pixel value distribution of the map for the PSF-photometry.

### 2.3. Final uncertainty and *Herschel* flux

As the observations are centred at the position of the radio galaxies, which are well detected at shorter wavelength, we have a strong prior on the detection of a source at a given position. We define “strict non-detection”, “tentative detection” and “strong detection” as sources detected at the  $F^{\text{gal}} < 2\sigma$ ,  $2\sigma < F^{\text{gal}} < 3\sigma$  and  $F^{\text{gal}} > 3\sigma$  levels, respectively.

In the case of a non-detection ( $F^{\text{gal}} < 2\sigma$ ), we took the upper limit as three times the sky standard deviation (we discussed the estimation of the uncertainties in previous sub-sections). In the case of tentative detection ( $2\sigma < F^{\text{gal}} < 3\sigma$ ), we provide the value of the flux between square brackets (Table 3) and display these as open diamonds on the SED plots (Fig. D.1). In addition, we add the calibration uncertainty in the formal errors for detected sources. Table 3 presents the final flux estimates and their associated total uncertainties (photon, instrumental and confusion noise). They are calculated by adding quadratically the absolute calibration uncertainty (see Table 2) with the uncertainty estimated directly from the noise characteristics of the images (Section 2.2.3). Because of the additional flux calibration uncertainty, the *Signal-to-noise* ratio does not correspond to the flux uncertainties given in Table 3, as those are calculated *before* applying the calibration correction.

### 2.4. Sub-mm data, LABOCA

In addition to the fluxes already available in the literature (Archibald et al., 2001; Reuland et al., 2003), we obtained new sub-mm data for some of those sources lacking it<sup>3</sup>. We observed 18 sources in the southern hemisphere spanning  $1 < z < 3$ . The observations were done in service mode between 2012 July and December, with precipitable water vapour generally below 1 mm. To save observing time, most sources were observed using the LABOCA wobbler on-off (WOO) photometry mode. As this WOO mode does not provide any spatial information, it should only be used on isolated sources. If the *Herschel* maps showed either multiple point-like sources within a radius of 20'' (one LABOCA beam size), or a spatial offset more than 5'' from

<sup>3</sup> Based on observations made with APEX telescope obtained during ESO, Chile and Sweden time under programme IDs E-090.A-0730. APEX is a collaboration between the Max-Planck-Institut für Radioastronomie, the European Southern Observatory, and the Onsala Space Observatory.

the radio core position, we used the raster spiral mapping mode instead. The integration times per source were adapted to obtain an approximately uniform rms for all 18 sources. To reduce the data, we used the doOO script inside BoA (Schuller, 2012) for the WOO data, and the reduction macro in CRUSH2 (Kovács, 2008) for the mapping data. Table 4 summarises the observing modes, fluxes, uncertainties and the references for data taken from the literature.

### 3. The HeRGÉ Infrared Spectral Energy Distributions

Combining the *Spitzer*, *Herschel* and sub-mm data, we continuously cover the wavelength range 16–870  $\mu\text{m}$ . The panels of Fig. D.1 show the resulting SEDs for our 70 radio galaxies. As our focus is on the warm to cold dust emission, we do not use *Spitzer* IRAC photometry in our SEDs because those data are generally dominated by stellar photospheric emission (e.g. Seymour et al., 2007). De Breuck et al. (2010) show that hot dust emission can also contribute significantly to the IRAC fluxes of some sources. This hot dust component ( $>500\text{ K}$ ), however, only represents a small fraction of energy of the total IR SED ( $<5\%$ ), and is influenced by orientation-dependent effects (Drouart et al., 2012). We therefore do not include this hot dust contribution in our SED fitting. Moreover, we add 20% uncertainties to the MIPS data to account for cross-calibration uncertainties between *Spitzer* and *Herschel*. We overplot the *Spitzer* spectrum available for a sub-sample of our sources (Seymour et al., 2008; Rawlings et al., 2013). These spectra are not used to constrain our fits, but provide a consistency check on our decomposition of the IR/submm SEDs.

#### 3.1. Total IR luminosities

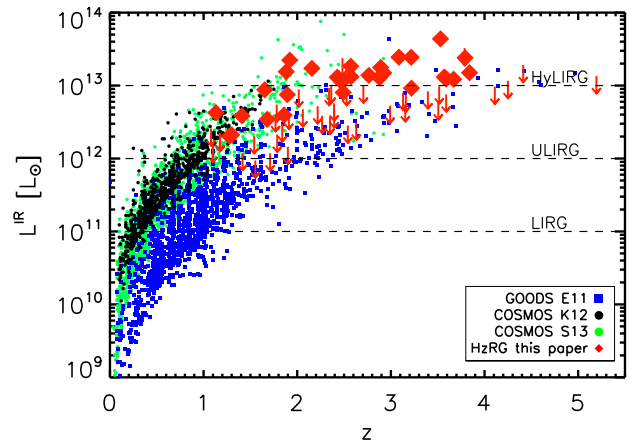
Since our IR/submm SEDs are well-sampled, we can estimate robustly the total IR luminosity ( $L_{\text{tot}}^{\text{IR}}$ ). We use its most common definition, integrating the flux density in the 8–1000  $\mu\text{m}$  rest-frame range. To interpolate between our photometric data points, we assume the models described in § 4. From these estimates of the total IR luminosity, it appears that almost all radio galaxies from our sample are ultra-luminous infrared galaxies (ULIRG;  $L_{\text{obs}}^{\text{IR}} > 10^{12} L_{\odot}$ ).

Fig. 1 plots our sample along with other samples available in literature with *Herschel* observations. Our galaxies are among the brightest emitters in the IR in their redshift range. About half of our  $z > 2$  sample belongs to the HyLIRG regime ( $L_{\text{tot}}^{\text{IR}} > 10^{13} L_{\odot}$ ). From this diagram, it is interesting to note that the high redshift radio galaxies are indistinguishable from the most extreme IR emitters.

Interestingly, such luminous objects imply strong AGN and/or star formation activities. This should be compared with previous results about the mass of these objects, located at the high-mass end of the galaxy mass distribution (e.g. Rocca-Volmerange et al., 2004; Seymour et al., 2007). Even if these galaxies are identified as the progenitors of the “red-and-dead” local ellipticals (e.g. Matthews et al., 1964; Rocca-Volmerange et al., 2004; Thomas et al., 2005; Labbé et al., 2005), they appear to be pretty active in the past.

#### 3.2. The warm and cold dust contributions

While both AGN and SB can heat dust, their input SEDs are significantly different. AGN heating tends to contribute at



**Fig. 1.** Total IR luminosity ( $L_{\text{tot}}^{\text{IR}}$ ) versus redshift. The green dots are the COSMOS sample from Kartaltepe et al. (2010), using *Spitzer* data. The blue squares are the GOODs samples from Elbaz et al. (2011). The black dots are the selection from Symeonidis et al. (2013). We also indicate the LIRG, ULIRG and HyLIRG limits.

shorter wavelengths ( $\sim 10\text{ }\mu\text{m}$ ,  $T_{\text{dust}}^{\text{AGN}} \sim 300\text{ K}$ ) while star formation heating tends to dominate the emission at longer wavelengths ( $\sim 100\text{ }\mu\text{m}$ ,  $T_{\text{dust}}^{\text{SB}} \sim 30\text{ K}$ ). Given the large variety of the data quality, we want to define a set of criteria to disentangle the AGN and SB contributions. We therefore classify our galaxies into classes depending on the number of detections on either side of 50  $\mu\text{m}$  restframe (e.g. Leipski et al., 2013). This value is preferred for several reasons. First, in the case of an object with both contributions (AGN and SB), the change in regime is expected to occur around this wavelength. Second, our sample spans a large range in redshift ( $1 < z < 5$ ) and therefore a simple colour selection would be severely affected by the  $k$ -correction. Third, this wavelength equally splits the number of channels available for each source (four bands on either side). We note that by changing this limit to 30  $\mu\text{m}$  or 70  $\mu\text{m}$  only changes the fraction of sources in each class by a small amount ( $<5\%$ ).

The classes are defined as follows, with their respective fractions in our sample:

1. **Warm and cold dust (WCD, 45%)**: corresponds to detections on both sides of  $\lambda_{\text{rest}} = 50\text{ }\mu\text{m}$ .
2. **Warm dust (WD, 33%)**: corresponds to detections only in the mid-IR ( $\lambda_{\text{rest}} < 50\text{ }\mu\text{m}$ ).
3. **Cold dust (CD, 11%)**: corresponds to detections only in the far-IR ( $\lambda_{\text{rest}} > 50\text{ }\mu\text{m}$ ).
4. **Upper Limit (UL, 11%)**: corresponds to no detections in either the mid-IR or the far-IR.

We detect warm, *preferentially* AGN-heated dust emission in the majority (78%) of our sample, while the cooler, *preferentially* starburst-heated dust emission is detected in half (54%) of our sample (Table 6). This difference between the possible constraints on the two components can be interpreted in two ways: either our *Herschel* (and in particular SPIRE) data are comparatively less sensitive than *Spitzer*, or the AGN contributes more significantly to the IR SED while the strength of the associated SB varies by a larger amount. We note that only 11% of our sample does not have any constraints on the relative contributions of either AGN or starbursts to the IR SED.

To further examine correlations involving IR luminosities in our sample, we next separate the AGN and SB components.

#### 4. IR SED Decomposition Method

In order to decompose the two main contributions to the IR SED, AGN and SB emission, we need models for each component. The AGN dust emission, which contributes mainly in mid-IR emission, comes mainly from the far-UV through optical light that has been reprocessed by dust in close proximity to the AGN. The far-UV through optical emission from any young stellar population that may exist is largely reprocessed into the far-IR via dust grains.

One of the most important goals of this analysis is to determine the relative emission from the AGN and starburst components. Disentangling this relative emission allows us to investigate the principal physical processes responsible for the luminous IR emission in distant radio galaxies, since the dust reprocessed emission is the largest contributor in active galaxies. Such analysis provides the best measure of the bolometric luminosity.

We use the SED fitting procedure *DecompIR* (Mullaney et al., 2011, <https://sites.google.com/site/decompir/home>), with some minor modifications to add the information and constraints provided by the *Herschel* and sub-mm data. Briefly, *DecompIR* allows the fitting of one or two templates thanks to  $\chi^2$  minimisation. It considers an empirical library estimated from local starburst and an empirical unique AGN template consisting of a composite spectrum of broken power-laws and a black body. All templates cover the 3-1000  $\mu\text{m}$  rest-frame range<sup>4</sup>, and an extinction can be applied independently for each component. This procedure has been extensively tested on higher redshift sources and described in Del Moro et al. (2013). In order to keep our approach as homogeneous as possible over the whole sample, we minimize the number of free parameters. We remind the reader that we did not include the IRAC data because it contains a significant component of stellar photospheric emission.

##### 4.1. Additional starburst template

*DecompIR* includes five different SB templates. Briefly, they represent SB with different peaking temperatures and PAH strength, with the coldest corresponding to SB1. We refer to Mullaney et al. (2011, their Fig. 4) for presentation of the SEDs. For two galaxies (*4C 41.17* and *4C 28.58*), these five available templates do not converge to an acceptable solution. The best fitting SED suggests that either a hotter starburst component or a colder AGN contribution (Figure D.1) is required to reproduce the observed SED. However, *4C 41.17* is well fitted by a synthetic SED from the galaxy synthesis and evolution code, PEGASE.3 (Rocca-Volmerange et al., 2013). Fortuitously, this galaxy appears to have a relatively small AGN contribution (Dey et al., 1997). Rocca-Volmerange et al. (2013) show that the IR part of the SED is clearly dominated by a young stellar population. We have therefore included the IR part of the best fitting SED of *4C 41.17* from PEGASE.3 as a new template to the *DecompIR* library (the “SB6” template). This template has the highest relative dust temperature of any of the SB templates

<sup>4</sup> Due to  $k$ -correction effects, a part of the IRS filter falls outside the template for  $z > 2.5$ . We therefore extrapolate the templates to  $\lambda = 2 \mu\text{m}$  using a power-law function. This modification does not impact our results as the energy contribution from these wavelengths ( $2 \mu\text{m} < \lambda < 3 \mu\text{m}$ ) is negligible compared to the total IR luminosity.

in the library – its dust emission peaks at  $\sim 60 \mu\text{m}$  ( $\sim 50\text{K}$ ). This template does not represent a local SB as the other templates, it is a solution for a 30 Myr old starburst (Rocca-Volmerange et al., 2013). However, we seek here only to reproduce the general shape of the IR SED to estimate IR luminosities, and will not make any further considerations about the age/mass of this template. A further analysis of the SB/host properties similar to the approach Rocca-Volmerange et al., 2013 is the object of a forthcoming paper (Drouart et al., in prep).

##### 4.2. AGN template

The AGN template used in this analysis is calculated using a sample of AGN that has had the starburst contribution removed from their mid-IR spectral energy distribution. The template is an average of the residual mid-IR SEDs (see Mullaney et al., 2011, for details). Due to the empirical nature of this subtraction and the variety of possible AGN-dominated mid-IR SEDs, this average template is expected to show discrepancies from object to object, however it represents well the average AGN spectrum in mid-IR (Dale et al., 2014). Ideally, we would like to use different AGN templates, similar to the SB analysis. In particular, the hottest part of the AGN is subject to inclination-dependent effects (e.g. Leipski et al., 2010; Drouart et al., 2012).

In order to test this, we modified *DecompIR* to include the average type 1 AGN template from Richards et al. (2006) onto which we apply an extinction from Fitzpatrick (1999). Even if this AGN template significantly improves our fitting, we decided to discard this template from our library for the following reasons. First, the inclusion of an extra parameter (the extinction) decreases the number of sources on which our fitting can be applied. Second, the Richards template presents an odd, and unrealistic tail in the far-IR (probably due to the poor far-IR coverage of the dataset used to build this template). Third, while increasing the scatter in  $L_{\text{AGN}}^{\text{IR}}$ , we find no drastically different results from using the built-in AGN template. Finally, being an average template, star formation can still contribute at long wavelength and we would therefore overestimate the AGN luminosity.

##### 4.3. Transition regime: hot starburst or cold AGN ?

The transition between the two components is the most critical parameter as it has an important influence on the calculated IR luminosities. On one hand, we want to be sure that the templates we are using are effectively representative of the AGN and/or the SB components. On the other hand, we want to keep the decomposition as simple as possible to apply it over the entire sample. As previously mentioned, we use only one AGN template, deemed representative of the general AGN SED. How can we be certain that this only empirical template is representative for all our sources? This question is difficult to answer as the data quality varies from object to object and we only have broad band photometry for our sample. Nevertheless, one can argue that this template is valid considering the following assumptions. The cold dust emission for the AGN ( $\lambda_{\text{rest}} > 30 \mu\text{m}$ ) can come from (i) an extended torus (e.g. Fritz et al., 2006; Nenkova et al., 2008), or (ii) reprocessed light from the NLRs (e.g. Dicken et al., 2009, 2010). While (i) will require the inclusion of a large number of new free parameters, (ii) can only be assessed by the [OIII] luminosities that are not available for our entire sample. The quantification of these effects is beyond the scope of this paper and will therefore be ignored for the remainder of the analysis. Moreover, one notes that the empiri-

**Table 5.** Distribution of the sample as a function of their class and their number of detections in the IR.

| Class | N. of Detections |   |    |   |   |   |   |   |   |
|-------|------------------|---|----|---|---|---|---|---|---|
|       | 0                | 1 | 2  | 3 | 4 | 5 | 6 | 7 | 8 |
| UL    | 8                |   |    |   | 1 |   |   |   |   |
| WD    |                  | 4 | 17 | 0 | 2 | 1 | 0 | 0 | 0 |
| CD    |                  | 5 | 1  | 1 | 1 | 0 | 0 | 0 | 0 |
| WCD   |                  |   | 1  | 3 | 2 | 6 | 6 | 6 | 5 |

cal AGN template does present a significant contribution at long wavelength. It is also interesting to note that the extreme object *4C 23.56* represents the prototype of a pure AGN contribution, and is remarkably well reproduced by the built-in template. Part of our sample (7 objects) have IRS spectra (12–24  $\mu\text{m}$ ) available (Seymour et al., 2008; Rawlings et al., 2013). Overplotting the spectrum *after* the fitting shows a good agreement between the IRS and the results. Finally, the overall results do not seem to bias our results towards one or another SB templates (see Table 6).

#### 4.4. AGN/SB relative contribution

The relative contribution of the AGN and the SB can vary a lot, depending of the physical condition of the SB or the configuration of the dust close to the AGN (see previous section). In order to check this potential impact on the previously defined classification (UL, CD, WD, WCD) we define three values of the relative AGN and SB contribution to the flux at 10, 50 and 100  $\mu\text{m}$  restframe ( $f_{\text{AGN}}^{10,50,100\mu\text{m}} = F_{\text{AGN}}^{10,50,100\mu\text{m}} / F_{\text{SB}}^{10,50,100\mu\text{m}}$ ). This relative contribution may vary, depending on the SB template used for the fit. In the mid-IR (10  $\mu\text{m}$ ), this effect can be strong due to the emission from Polycyclic Aromatic Hydrocarbon (PAH) molecules. For the two extreme starburst templates, this relative contribution can vary up to a factor of 4. Nevertheless, in most cases, we can discriminate between the most extreme templates (SB1 and SB5) which have a factor of  $\sim 2$  difference in their relative contributions for the same total luminosity. In the far-IR (100  $\mu\text{m}$ ) this relative difference is smaller, the SB dominates the SED except for a few cases (e.g. *4C 23.56*). The Appendix B shows these fractions as a function of the total infrared luminosity  $L_{\text{tot}}^{\text{IR}}$ .

#### 4.5. Procedure on the sample

The large difference in data quality prevents us from blindly applying the same fitting procedure on all galaxies in the full sample. In order to take full advantage of our data, we apply different procedures on each source, depending on the number and the quality of detections, and their previously defined classes (see § 3.2 and Tab. 5). We also highlight some special cases which need a specific treatment. We stress that independently from their designated class, each acceptable solution must respect the “3-sigma rule”: if a solution present a template brighter than any of our  $3\sigma$  detection limits, this solution was discarded as not physically acceptable. Note that all calculated infrared luminosities are integrated over the 8–1000  $\mu\text{m}$  range.

**UL sources:** For sources without any firm detections, only upper limits on  $L_{\text{AGN}}^{\text{IR}}$  and  $L_{\text{SB}}^{\text{IR}}$  can be calculated. We normalise separately the AGN template and a SB template on the most constraining upper limit. The upper limit on  $L_{\text{tot}}^{\text{IR}}$  is calculated by

fitting simultaneously both templates on the most constraining upper limits.

**WD sources:** For sources with detections only in the mid-IR, we fit only an AGN template. In a second step, we normalise a SB template to the most constraining upper limit in the far-IR. The upper limit on  $L_{\text{tot}}^{\text{IR}}$  is calculated fitting simultaneously both templates on the detected points in mid-IR and the most constraining upper limit in far-IR.

**CD sources:** For sources with detections only in the far-IR, we fit only an SB template. If the number of detections allows it ( $n \geq 2$ ), we leave the type (SB1 to SB6) as a free parameter. In a second step we normalise the AGN template on the most constraining upper limit in the mid-IR. The upper limit on  $L_{\text{tot}}^{\text{IR}}$  is calculated fitting simultaneously both templates on the detected points in the far-IR and the most constraining upper limit in the mid-IR.

**WCD sources** For sources with two or three detections in mid- and far-IR, we fit both AGN and SB components but choose the SB template which maximises  $L_{\text{tot}}^{\text{IR}}$  with respect to the most constraining upper limits in the far-IR. For sources with four or more detections, we fit both the AGN and SB components, with the SB type template as an additional free parameter in the fitting. In both cases,  $L_{\text{tot}}^{\text{IR}}$  is the sum of both templates. As mentioned previously, extinction could have a strong impact on the fitting. We tested for this effect on this subsample adding the extinction as a free parameter on both components. The  $L_{\text{SB}}^{\text{IR}}$  and  $L_{\text{AGN}}^{\text{IR}}$  are changed within a factor  $< 3$ . We therefore do not consider extinction in our fitting procedure for the remainder of this paper.

Table 6 provides the measured  $L_{\text{tot}}^{\text{IR}}$ ,  $L_{\text{AGN}}^{\text{IR}}$ ,  $L_{\text{SB}}^{\text{IR}}$  and SB template given by the best solution and the AGN fraction at 10, 50 and 100  $\mu\text{m}$  restframe. The AGN fractions are described in § 4.4 and Appendix B.

## 5. Results

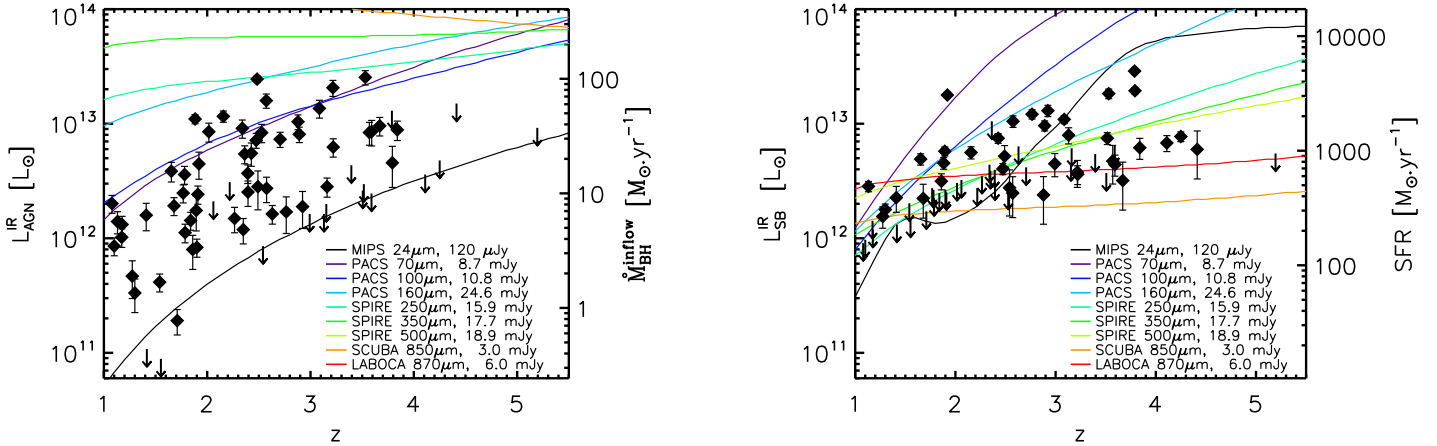
### 5.1. AGN/SB detection limits

Fig. 2 shows both the infrared AGN and SB luminosities as a function of redshift. In order to verify whether the upper limits on the AGN and the SB components are mainly due to physical processes or purely from an observational bias, we calculate the minimum luminosity for each component related to the band sensitivity. Our  $3\sigma$  sensitivity limits are calculated averaging the uncertainties over the entire sample. We normalise the AGN and SB3<sup>5</sup> templates in each observed band and calculate the corresponding  $L_{\text{AGN}}^{\text{IR}}$  or  $L_{\text{SB}}^{\text{IR}}$  at any redshift.

One notes that our upper limits do not always follow the most sensitive detection limit (for instance the black line on left plot). This can be explained as: (i) the IR emission is a mixture of AGN- and SB-heated dust; (ii) especially in the IR, the background emission varies locally and as a function of Galactic longitude, impacting the final sensitivity; (iii) the depth of the MIPS (24  $\mu\text{m}$ ) imaging is not uniform throughout the sample (De Breuck et al., 2010).

From these diagrams, MIPS 24  $\mu\text{m}$  data appear to be the most sensitive to the AGN contribution at any redshift. It is important to remember that a pure AGN contribution is very unlikely to be

<sup>5</sup> We note that using another SB template would introduce some variation but the general shape of the threshold remains unchanged.



**Fig. 2.** *Left:*  $L_{\text{AGN}}^{\text{IR}}$  against redshift. The ordinate on the right hand side of the plot is calculated using Eq. 2 assuming a radiative conversion efficiency  $\epsilon=0.1$  and  $\kappa_{\text{Bol}}^{\text{AGN}}=6$  (§ 6.1.2). *Right:*  $L_{\text{SB}}^{\text{IR}}$  against redshift. The ordinate on the right hand side of the plot is calculated using Eq. 1, assuming the Kennicutt (1998) law. We indicate our average  $3\sigma$ -sensitivity limit for the AGN and the SB3 templates for each filter (see § 5.1 for details, figure inspired from Elbaz et al. (2011)). One notes that in a case of pure AGN emission, MIPS (24  $\mu\text{m}$ ) is the most sensitive band over the entire redshift range. On the other hand, in the case of a pure starburst emission, the most sensitive band at  $z>2$  is in the submm (APEX or SCUBA).

detected in the sub-mm as they require AGN of  $L_{\text{AGN}}^{\text{IR}} > 10^{14} L_{\odot}$  at any redshift (see orange, SCUBA line at the top of Fig. 2, left). Nevertheless, one should be careful to associate the 24  $\mu\text{m}$  flux to the AGN because PAH contributions from star formation can be important in this band (see plateau in Fig. 2, right). In the case of a pure SB component, the situation is completely different. Up to  $z\sim 2$ , MIPS 24  $\mu\text{m}$  is again our most sensitive band to detect both SB and AGN. However, in the case of a pure SB component, the SB will be detected only at  $L_{\text{SB}}^{\text{IR}} > 10^{12} L_{\odot}$  where for the same sensitivity a pure AGN will be detected at the  $L_{\text{AGN}}^{\text{IR}} > 3 \times 10^{11} L_{\odot}$  level. This implies that the MIPS 24  $\mu\text{m}$  band is likely to be dominated by AGN emission if any hints of AGN activity is detected in a source (which is the case for radio galaxies).

At  $z>2$ , SCUBA (and LABOCA) become our most sensitive bands for detecting SB components. Moreover, due to  $k$ -correction effects (Blain et al., 1999), this limit is roughly constant with redshift. Our  $3\sigma$  sensitivity allows us to detect starburst activity of at least  $400 M_{\odot} \text{yr}^{-1}$  ( $800 M_{\odot} \text{yr}^{-1}$  for LABOCA) assuming the standard  $L_{\text{tot}}^{\text{IR}}$ -SFR conversion law (Kennicutt, 1998).

## 5.2. Infrared AGN and Starburst luminosities

Fig. 2 plots  $L_{\text{AGN}}^{\text{IR}}$  and  $L_{\text{SB}}^{\text{IR}}$  versus redshift. Both plots suggest an increasing trend with redshift ( $\rho=0.374$ ,  $p=0.0019$  and  $\rho=0.613$ ,  $p<0.0001$ , respectively<sup>6</sup>). While this trend seems real for  $L_{\text{AGN}}^{\text{IR}}$  (given the few upper limits), it appears stronger with  $L_{\text{SB}}^{\text{IR}}$ . Indeed, even if  $L_{\text{SB}}^{\text{IR}}$  is affected by numerous upper limits, especially at  $z<2.5$  (due to the limited sensitivity of the 250  $\mu\text{m}$  SPIRE band), these upper limits are fully consistent with an increasing trend. An improvement of one order of magnitude in our far-IR sensitivities should certainly be enough to detect the missing sources and therefore confirm the increasing trend with redshift for  $L_{\text{SB}}^{\text{IR}}$ .

<sup>6</sup> Making use of the IRAF survival analysis package,  $p$  is the probability of no correlation.

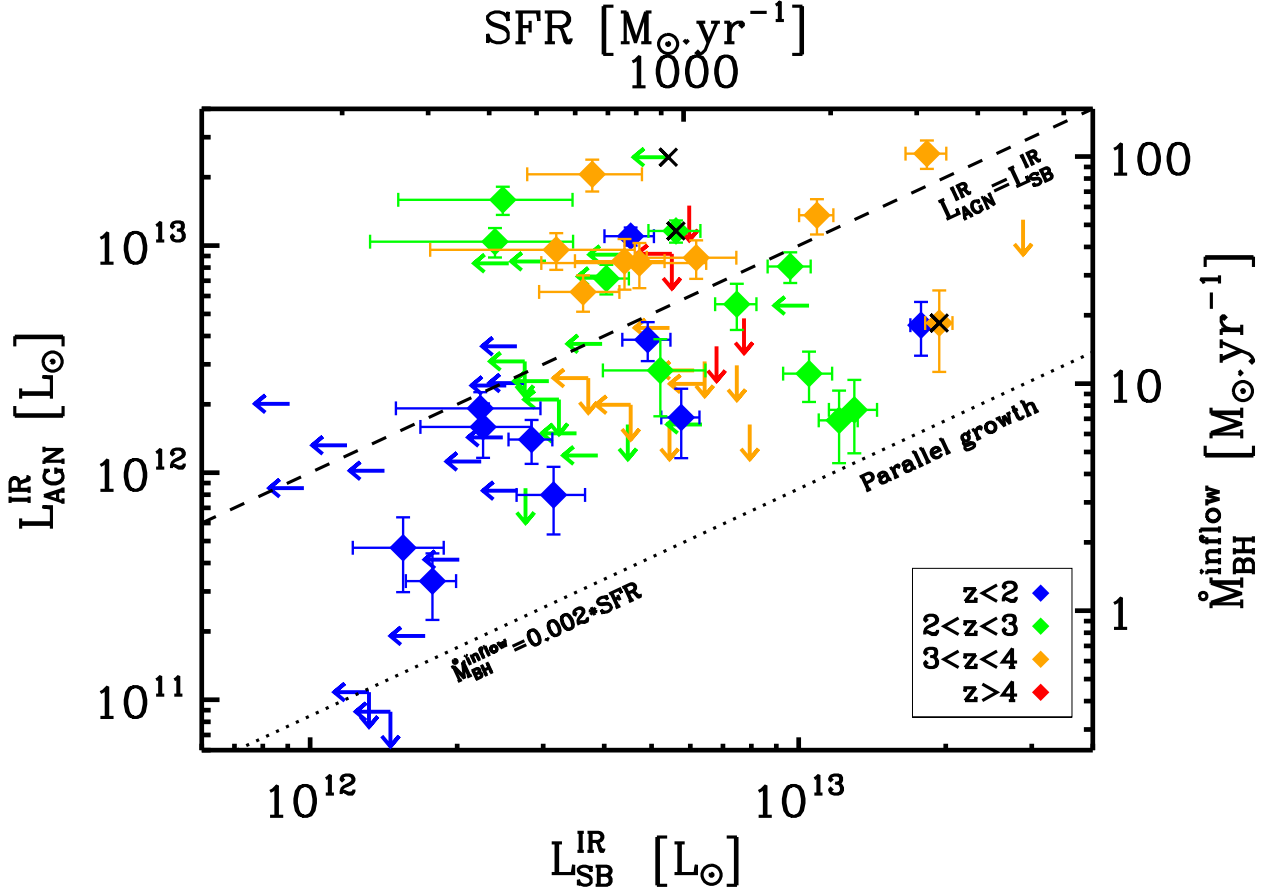
We also estimate the black hole accretion rate ( $\dot{M}_{\text{BH}}$ ) and the star formation rates (SFR) based on the fits to the SED. We discuss these parameters in greater detail in § 6. First, we note that our sample spans a large range in both SFR and  $\dot{M}_{\text{BH}}$ , almost two orders-of-magnitude for both of them,  $1 M_{\odot} \text{yr}^{-1} < \dot{M}_{\text{BH}} < 100 M_{\odot} \text{yr}^{-1}$  and  $100 M_{\odot} \text{yr}^{-1} < \text{SFR} < 5000 M_{\odot} \text{yr}^{-1}$ . Moreover, as they scale linearly with  $L_{\text{AGN}}^{\text{IR}}$  and  $L_{\text{SB}}^{\text{IR}}$ , the suggested increasing trend with redshift applies to both the SFR and the black hole accretion rate. In particular, all our  $z<2$  sources have a  $\dot{M}_{\text{BH}} < 5 M_{\odot} \text{yr}^{-1}$ , while at  $z>2$ ,  $\dot{M}_{\text{BH}}$  can reach  $100 M_{\odot} \text{yr}^{-1}$ . The same behaviour, though weaker, can be observed with SFR where all sources (except one) have  $\text{SFR} < 1000 M_{\odot} \text{yr}^{-1}$  at  $z<2.5$ , while SFR can reach  $4000 M_{\odot} \text{yr}^{-1}$  for the sources with the highest redshifts.

Fig. 3 plots  $L_{\text{AGN}}^{\text{IR}}$  versus  $L_{\text{SB}}^{\text{IR}}$  (we discuss this plot more extensively in § 6). Radio galaxies cover a wide range of relative contributions: from almost pure star forming galaxies (e.g. *4C 41.17*), to almost pure AGN contribution (e.g. *4C 23.56*<sup>7</sup>) but with the majority having SEDs which are composites of star formation and AGN heating (e.g. *PKS 1138-262*). We point these three specific sources in Fig. 3 as black crosses.

Taking into account only the objects with good constraints on both their AGN and SB contributions, we find no significant correlation. This provides confidence about the decomposition as we do not expect, *a priori*, to have a correlation between the AGN and SB luminosities (as also find in other studies, e.g. Bongiorno et al., 2012; Dicken et al., 2012; Feltre et al., 2013; Leipski et al., 2014). Nevertheless, it is interesting to note that each component (AGN and SB) has an integrated luminosity of  $L^{\text{IR}} > 10^{12} L_{\odot}$ . This indicates that a high IR luminosity does not necessarily imply a high star formation rate or a strong AGN activity.

<sup>7</sup> classified as a WD, this extreme object appears to be the prototype of the pure AGN contribution (c.f. Appendix A and Fig. D.1).





**Fig. 3.**  $L_{\text{AGN}}^{\text{IR}}$  versus  $L_{\text{SB}}^{\text{IR}}$ . The top axis converts  $L_{\text{SB}}^{\text{IR}}$  to SFR using the Kennicutt (1998) relation (Eq. 1). The right axis converts  $L_{\text{AGN}}^{\text{IR}}$  to  $\dot{M}_{\text{BH}}$  assuming  $\epsilon=0.1$  and  $\kappa_{\text{AGN}}^{\text{Bol}}=6$  (Eq. 2). The dashed line marks  $L_{\text{AGN}}^{\text{IR}}=L_{\text{SB}}^{\text{IR}}$ . This dashed line indicates the relation corresponding to  $\dot{M}_{\text{BH}}=0.024 \times \text{SFR}$ , using the right and top axis. The dotted line represents the parallel growth mode, where black holes and galaxies are growing simultaneously, following the  $M_{\text{BH}}-M_{\text{Gal}}$  relation (see § 6.1.3 for details). Colours code redshift bins. The three crosses indicate the three sources of peculiar interest, *4C 23.56*, *PKS 1138-262* and *4C 41.17*

### 5.3. Comparing AGN and SB IR luminosities with radio properties

#### 5.3.1. Radio luminosities

De Breuck et al. (2010) calculated the 500 MHz restframe luminosity for the entire sample. In the case of powerful radio galaxies, the radio emission is dominated by the AGN. The 500 MHz luminosity ( $\nu 500$ ) is an excellent proxy for estimating the energy injected by the AGN into the lobes of the radio galaxy<sup>8</sup>.

We see a weak correlation over 2 orders of magnitude in  $L_{\text{AGN}}^{\text{IR}}$  and  $\nu 500$  (Fig. 4,  $\rho=0.475$ ,  $p=0.0001$ ). However, both  $\nu 500$  and  $L_{\text{AGN}}^{\text{IR}}$  present a correlation with redshift. As we constrained  $L_{\text{AGN}}^{\text{IR}}$  for most of our sample and  $\nu 500$  is well determined, we apply a partial correlation test<sup>9</sup> in order to take this mutual dependence on redshift into account. Indeed, this partial test severely

<sup>8</sup> At 500 MHz, the radio emission is dominated by the lobes. At such frequencies, relativistic beaming effects are not playing a significant role (Blundell et al., 1998).

<sup>9</sup> We make use of the IDL function *p\_correlate* and only consider sources with detected  $L_{\text{AGN}}^{\text{IR}}$  and  $\nu 500$ .

degrades the correlation ( $R=0.10$ ) indicating that redshift is the determinant factor of this correlation. It is therefore impossible to conclude much about the correlation between the radio and the IR in radio galaxies (at least with this sample which spans a wide redshift range but  $<2$  orders of magnitude in radio luminosity).

This apparent lack of correlation can be easily explained by comparing the timescales in the IR and radio to respond to changes in the energy output of the AGN. The dust heated by the AGN is likely to be circumnuclear given its emission temperature. Dust cools quickly and the timescale for the photons to stream through the nebula is relatively short. The radio emission, on the other hand, has a much longer response time to changes in the AGN output and the aging time of electrons is of the order of tens of Myr (Blundell et al., 1999), especially at low frequencies and considering shock re-energization in the lobes themselves. Also, it is not clear if the relative fraction of energy and emission in the radio and IR should be similar anyway.

$L_{\text{SB}}^{\text{IR}}$  and  $\nu 500$  tend to also present a positive weak correlation ( $\rho=0.536$  and  $p=0.001$  applying a survival analysis), similarly to  $L_{\text{AGN}}^{\text{IR}}$  and  $\nu 500$ . The numerous upper limits and poor statis-

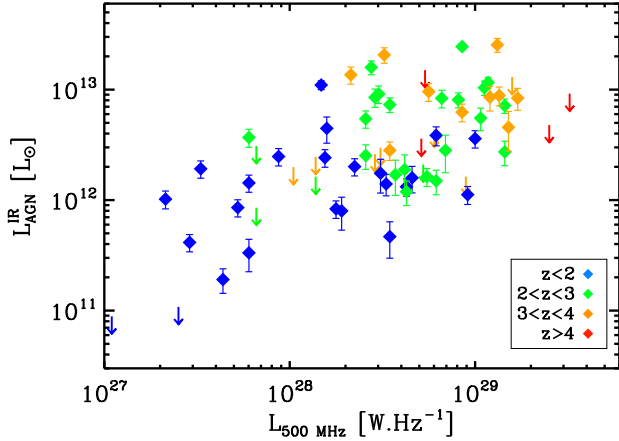


**Fig. 4.**  $L_{\text{AGN}}^{\text{IR}}$  against  $\nu 500$ . The colours code the redshift bins.

tics make it even more difficult to conclude anything about this correlation. Moreover, as for  $L_{\text{AGN}}^{\text{IR}}$ , this correlation seems also mostly driven by redshifts effects.

### 5.3.2. Radio sizes

Spatially resolved radio observations can measure the distance between the core and the lobe (or lobe-lobe), providing useful information on the age of the radio phase assuming a simple ballistic trajectory for the ejected particles (Blundell et al., 1999). The radio size,  $l_{\text{as}}$  (Table 2 in De Breuck et al., 2010), corresponds to the largest extension in 1.4GHz radio maps. As all our radio galaxies have a spectroscopically determined redshift, we calculate the projected size  $D\sin(i)$  in kpc of the radio galaxy where  $D$  is the physical size of the galaxy and the  $\sin(i)$  term refers to its projection onto the sky plane. A degeneracy appears here due to the inclination  $i$  of the radio galaxy. Nonetheless, this latter quantity is not expected to be important, as we are dealing with type 2 AGN, i.e. mostly oriented in the plane of the sky (Drouart et al., 2012). The real size  $D$  will likely be at most 30% larger due to projection effects.

Fig. 5 plots  $L_{\text{AGN}}^{\text{IR}}$  against the projected size  $D\sin(i)$ . Similar to  $\nu 500$ , coloured points show a redshift effect in our data; the most compact AGN are at higher redshift. Radio sizes could be also affected by two effects: (i) it can depend on environment (e.g. Kaiser et al., 1997; Klamer et al., 2006; Bornancini et al., 2010; Ker et al., 2012); and (ii) our sample presents a weak selection bias in size, with larger objects located at lower redshift (see Fig. 5).

### 5.4. Comparing IR luminosity with stellar mass

Our sample benefits from stellar mass estimates thanks to *Spitzer* data. By fitting the 3.6-24  $\mu\text{m}$  range with a sum of an elliptical template from PEGASE.2 (Fioc & Rocca-Volmerange, 1997) and blackbodies at various temperatures, De Breuck et al. (2010) estimated reliable stellar masses for our sample, finding values of  $\sim 10^{11-12} M_{\odot}$ . Although massive, our low dynamic range in mass prevents us from drawing any conclusion about possible correlations. However, it is interesting to note the large scatter in the AGN luminosity, over two orders of magnitude, but the relatively small scatter in  $M_{\text{stel}}$  (see Fig. 5 in De Breuck et al., 2010). Plotting  $M_{\text{stel}}$  against  $L_{\text{SB}}^{\text{IR}}$  exhibits the same behaviour,

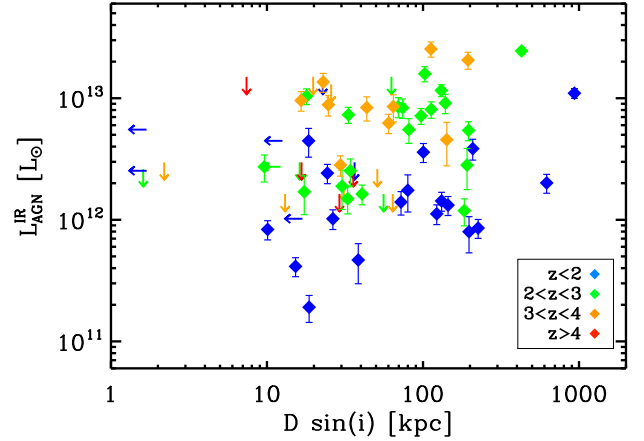


**Fig. 5.**  $L_{\text{AGN}}^{\text{IR}}$  versus projected size  $D\sin(i)$ . See § 5.3.2 regarding the details of the calculation of the projected size. The colours code redshift bins.

with the range of  $L_{\text{SB}}^{\text{IR}}$  being smaller given the larger number of upper limits. It is interesting to compare these masses and  $L_{\text{SB}}^{\text{IR}}$  with SMGs at similar redshift. While the SFRs are similar (e.g. Archibald et al., 2001; Reuland et al., 2004; Engel et al., 2010, § 6.1.1), our sample of radio galaxies appears more massive by a factor of 2-5 (De Breuck et al., 2010; Hainline et al., 2011; Michalowski et al., 2012; Simpson et al., 2013).

## 6. Discussion

Having disentangled the total IR luminosities of the star formation and AGN components in the SEDs, we can now estimate star formation rates (SFR), because we have stellar mass estimates ( $M_{\text{stel}}$ ), the specific star formation rates (sSFR), the black hole accretion rates ( $\dot{M}_{\text{BH}}$ ), Eddington ratios ( $\lambda$ ) and the specific black hole growth rates ( $s\dot{M}_{\text{BH}}$ ). Indeed, these estimates will allow us to characterize the evolutionary state of powerful radio galaxies, since we have a sample which spans a wide range of redshifts.

Are the host galaxies and their black holes co-evolving or is one of them outgrowing the other? Because it is difficult to provide reliable uncertainties for individual sources and parameters and undoubtedly our estimates suffer from systematic uncertainties, we will have to interpret these estimates as ensemble averages instead of focusing on individual measurements. With these insights, we will attempt to characterize the place of radio galaxies in the population of distant galaxies and what their future evolution might be within the context of their place in the ensemble population of galaxies.

### 6.1. How rapidly are radio galaxies and their black holes growing?

To put the radio galaxies into the context of the evolution of galaxies and into the broad range of black hole demographics (i.e. growth rate and masses), we need to convert estimates of the bolometric luminosities of both the recent star formation and the black hole accretion,  $L_{\text{SB}}^{\text{IR}}$  and  $L_{\text{AGN}}^{\text{IR}}$ , into SFR and  $\dot{M}_{\text{BH}}$ . These estimates depend on the rate at which short wavelength emission (e.g. blue optical, UV) from young stars is reprocessed into the IR and submm and the rate at which the accreted mass on to the

black hole is converted into radiated energy and the ratio of the IR luminosity to the total bolometric luminosity.

### 6.1.1. Star formation rate

We have found that powerful radio galaxies are extremely bright in the IR ( $L_{\text{tot}}^{\text{IR}} > 10^{12} L_{\odot}$ ), which may indicate that they have very high SFRs. We have seen in § 5.2 that we can disentangle SB from AGN emission. We can thus provide much more reliable determinations (e.g. Archibald et al., 2001; Reuland et al., 2004). Given the high IR luminosities and the fact that we are concerned here with the ensemble properties (averages, ranges, changes with redshift) not the details of individual sources, we will use the simple relation between the SFR and IR luminosity given for local galaxies (Kennicutt, 1998):

$$\text{SFR} = 1.72 \cdot 10^{-10} \times L_{\text{SB}}^{\text{IR}}, \quad (1)$$

where  $L_{\text{SB}}^{\text{IR}}$  is in units of  $L_{\odot}$  and SFR in  $M_{\odot}\text{yr}^{-1}$ . Our galaxies span a large range of SFR, from 100 to  $\sim 5000 M_{\odot}\text{yr}^{-1}$ . These results are similar to SFRs estimated for SMGs over the same redshift range (e.g. Engel et al., 2010; Wardlow et al., 2011; Swinbank et al., 2013) and radio galaxies from the 3C catalogue (e.g. Barthel et al., 2012)<sup>10</sup>. This wide range of SFRs is somewhat surprising. Radio galaxies obviously have very active and luminous AGN which emit across the electromagnetic spectrum and as such, the AGN must have a significant impact on the host galaxy. However, despite the evidence for the impact of the AGN, these galaxies exhibit a very wide range of SFR which is not correlated with the AGN luminosity (see Fig. 3). One must be very careful about both correlation or lack of correlation being causal, the fact that global star formation and AGN activity occur over different timescales, and that estimates of the instantaneous power output of an AGN may not be closely related to its longterm average (Hickox et al., 2013; Chen et al., 2013). Such variations might mask any underlying relationship.

None of the radio galaxies at  $z < 2.5$  (except one) show a high  $L_{\text{SB}}^{\text{IR}}$  and hence a high SFR compared to radio galaxies at higher redshifts (Fig. 2). The brightest IR sources, have SFRs up to  $5000 M_{\odot}\text{yr}^{-1}$ . Whether or not this is a physical limit (e.g. Lehnert & Heckman, 1996), we caution that this large value may be partially a result of the low angular resolution of our submm data ( $\sim 20$  arcsec at  $850 \mu\text{m}$ ). At  $z > 1$ , 20 arcsec corresponds to  $\sim 160$  kpc and so our observations may include contributions from many nearby star forming galaxies (e.g. Hatch et al., 2008; Ivison et al., 2008, 2012). The SFRs we have estimated are therefore in some cases best thought of as an upper limit to the SFR of the radio galaxy itself. If indeed several sources are in the same beam, the low resolution means that we are measuring an upper envelope of the SFR for the whole system (e.g. Karim et al., 2013). The multi-object nature of some IR sources is evident in recent ALMA high resolution observations of submm galaxies (Hodge et al., 2013). The overall similarity in the star formation rate estimates for our radio galaxies and the SMG population suggests that perhaps the most luminous radio galaxies are affected in the same manner. However, this is unlikely to be more than a factor of a few (Karim et al., 2013).

<sup>10</sup> We note that the  $L_{\text{SB}}^{\text{IR}}$  and SFR from our SED decomposition are also compatible with the previous estimates based on IRS spectra Seymour et al. (2008); Rawlings et al. (2013).

### 6.1.2. Black hole accretion rate

Assuming a fraction of the rest-mass energy of the material accreting onto the black hole is converted into radiation over the whole of the electromagnetic spectrum, one can estimate the accretion rate from an estimate of the bolometric luminosity. The accretion rate ( $\dot{M}_{\text{BH}}$ ) can be defined as:

$$\kappa_{\text{AGN}}^{\text{Bol}} \times L_{\text{AGN}}^{\text{IR}} = \epsilon \dot{M}_{\text{BH}}^{\text{acc}} c^2, \quad (2)$$

where  $\epsilon$  is the efficiency factor for converted accreted mass into bolometric luminosity and  $\kappa_{\text{AGN}}^{\text{Bol}}$  is a bolometric correction factor to convert  $L_{\text{AGN}}^{\text{IR}}$  into  $L_{\text{AGN}}^{\text{Bol}}$ . There are only a small number of empirical constraints on  $\epsilon$ . Results on quasar clustering suggest  $\epsilon > 0.2$  (Shankar et al., 2010; Shen et al., 2007), other studies suggest a mass-dependent factor ranging from 0.06 to 0.4 (Davis & Laor, 2011; Cao & Li, 2008; Volonteri et al., 2007; Merloni et al., 2004). We adopt here a conservative value of  $\epsilon = 0.1$ . If  $\epsilon$  is actually higher than our preferred value, all the relations will move by the necessary factor. The  $\kappa_{\text{AGN}}^{\text{Bol}}$  correction is uncertain, as it depends mostly on how much of the radiative energy is re-processed by dust, the wavelength of the observations that must be converted to the bolometric luminosity, and the AGN type and their selection (X-ray AGN, quasars, etc.). This conversion factor to the bolometric luminosity can vary from 1.4 to 15 for the IR (see Appendix C). Assuming the full unobscured AGN SED is similar to the Elvis et al. (1994) or Richards et al. (2006) templates, we find  $L_{\text{AGN}}^{\text{Bol}} \approx 6 \times L_{\text{AGN}}^{\text{IR}}$  (we note other unobscured AGN templates produce similar numbers). We therefore decided to fix  $\kappa_{\text{AGN}}^{\text{Bol}} = 6$ . We mark the influence of this choice with a vector in the relevant figures.

Similar to the star formation rates, the black holes in powerful radio galaxies appear to have a wide range of accretion rates,  $1\text{--}100 M_{\odot}\text{yr}^{-1}$  and similarly cover about two orders-of-magnitude (Fig. 2). To put this in perspective, powerful radio galaxies have accretion rates similar to those of high redshift quasars (Hao et al., 2008). Moreover, the accretion rates also appear to increase with redshift as do the star formation rates (Fig. 2).

Assuming  $\epsilon$  and  $\kappa_{\text{AGN}}^{\text{Bol}}$  are constant for the ensemble of radio galaxies,  $\dot{M}_{\text{BH}}$  also appears as an upper limit of accretion rates in these radio loud AGN. A simple order-of-magnitude calculation suggests that  $\sim 10^{7\text{--}9} M_{\odot}$  of gas is needed to continuously support such AGN activity over a 10 Myr timescale. This quantity of gas is similar to the gas mass observed at  $< 1$  kpc scale in some early-type gas-rich galaxies at low redshift (e.g. Young et al., 2011; Crocker et al., 2011). At higher redshift, where more molecular gas is expected to be present to fuel both the AGN and the star formation activity, only a few percent of the available gas mass observed in radio galaxy systems ( $\sim 10^{10\text{--}11} M_{\odot}$ , Ivison et al., 2012; Emonts et al., 2011, 2013) is necessary to fuel the central black hole. This transport of the gas to the inner part of the galaxy needs a process to efficiently remove the angular momentum of the gas to fall within the sphere of influence of the central black hole (e.g. Jogee et al., 2005). Even if some hypotheses are proposed, the dominant process is still unclear (e.g. Alexander & Hickox, 2012, for a review).

### 6.1.3. Co-eval stellar population and black hole growth?

How do the growth rates of the stellar population compare to that of the AGN in these powerful radio galaxies? If the galaxies and super massive black holes were growing sufficiently rapidly to remain on the spheroid mass-black hole mass relation, we would

expect the growth rate of the BH (i.e.  $\dot{M}_{\text{BH}}$ ) to be about 0.2% of the growth rate of the stellar population (i.e. SFR). However, with the parameters given in the previous two subsections, we find high redshift powerful radio galaxies are found to lie around the relation represented by  $M_{\text{BH}} = 0.024 \times \text{SFR}$  (i.e. offset by one order-of-magnitude, Fig. 3). Although obviously these estimates are very uncertain for individual sources, we see that overall, radio galaxies represent a phase in the evolution of both the galaxy and the black hole where relatively speaking, it appears as a more important growth of the black hole. In fact, it appears that the black hole is out-growing its host galaxy, in spite of the high observed SFR (similar to SMGs at similar redshift Alexander et al., 2005), by about a factor of 10 relative to what would be expected if they were growing in lock step. It is important to keep in mind that we set  $\kappa_{\text{AGN}}^{\text{Bol}} = 6$  and the exact value of the offset between the relative rate of black hole to galaxy growth is dependent on this choice. However, even if we choose a lower but still reasonable value, say  $\kappa_{\text{AGN}}^{\text{Bol}} = 2$  (see Appendix C), the general population of powerful radio galaxies would still have a significant offset toward more rapid black hole growth.

We also stress that this result is completely mass-independent, as neither the mass of the black hole nor of the galaxy are needed, only the local spheroid mass-black hole mass to draw the parallel growth mode (dotted line in Fig. 3). This behaviour is similar to moderate redshift quasars ( $z=1$ , Urrutia et al., 2012) and high redshift quasars ( $z=6$ , Willott et al., 2013). This similarity suggests that high accretion rates are more directly related to the fact that the AGN are bolometrically luminous with copious output rates of ionizing photons but are not directly related to the production of the powerful radio emission in the extended radio lobes (see § 5.3). Notably, the presence of strong emission lines in our sample of radio galaxies (e.g. Vernet et al., 2001; De Breuck et al., 2002) suggests that these powerful radio galaxies have indeed high relative accretion rates (e.g. Janssen et al., 2012; Hardcastle et al., 2007) as expected if the black holes are growing rapidly as we purport. We remind the reader, as discussed earlier, the calculated  $\dot{M}_{\text{BH}}$  represents the instantaneous accretion rate of the BH, not the long term average accretion rate. Variability in the bolometric luminosity and hence the accretion rate may be important (Hickox et al., 2013). However, such an effect is not likely to be important for the ensemble since the mean will remain the same, variability will only introduce more scatter.

## 6.2. Black hole mass and Eddington ratio

There are black hole mass estimates for five of our objects from broad components of the  $\text{H}\alpha$  emission (Nesvadba et al., 2011). They show that the black holes in powerful radio galaxies are extremely massive,  $M_{\text{BH}} > 10^9 M_{\odot}$ . Only based on this small number, a characterisation of the black holes properties over our entire sample is difficult. However, these measurement are especially useful for comparison with the assumptions in the following sections.

To increase the number of  $M_{\text{BH}}$  estimates, we will use empirical relationships based on both  $M_{\text{stel}}$  and  $L_{\text{AGN}}^{\text{IR}}$  to estimate the black hole mass in our sample. These two approaches are somewhat degenerate, as they are using the same data, with two different sets of assumptions. We first define the assumptions made in using the total stellar mass and the local  $M_{\text{BH}}-M_{\text{bulge}}$  relation to estimate black hole masses. We then use the infrared luminosity of the AGN combined with this mass to calculate the Eddington ratio. We also present a second approach where we fix the Eddington ratio ( $\lambda=0.1$ ) and then use the infrared luminosity

of the AGN to estimate the black hole mass. We took these two approaches to constrain the possible ranges for the Eddington ratios and/or black hole masses and to isolate the impact of the various assumptions that go into these sorts of estimates. We also mention the systematics that would affect our results when relevant, and summarise them in Appendix D.

### 6.2.1. Black hole mass

As previously noted, all the galaxies in our sample have estimated stellar masses (Seymour et al., 2007; De Breuck et al., 2010). All are very massive, with  $M_{\text{stel}} > 10^{11} M_{\odot}$ . When *HST* imaging is available, the best fit light profiles are consistent with  $n=4$  profile (Pentericci et al., 2001, Appendix D), suggesting that the luminosity weighted mass distribution has a spheroidal morphology (even if some discrepancies are observed). Since the mass of the black hole is related to the spheroidal mass<sup>11</sup>, we can use the local  $M_{\text{BH}}-M_{\text{bulge}}$  relationship to estimate the black hole mass,  $M_{\text{BH}}$  (Häring & Rix, 2004):

$$\log_{10}(M_{\text{BH}}/M_{\odot}) = 8.2 + 1.12 \log_{10}(M_{\text{bulge}}/10^{11} M_{\odot}), \quad (3)$$

where  $M_{\text{BH}}$  and  $M_{\text{bulge}}$  are in  $M_{\odot}$ . We therefore refer to this approximation as the local approximation (see Fig. 6, left).

Out of the five sources in our sample with independent black hole mass estimates, only one  $M_{\text{BH}}$  is directly comparable given the upper limits on the stellar mass (due to AGN torus contribution in the other 4 sources in the near-IR). For this source, *MRC 0156-252*, the derived  $M_{\text{BH}}$  from stellar mass lies at a factor  $\sim 4$  below that estimated using the broad  $\text{H}\alpha$  emission. The four remaining sources suggest also a significant offset in respect to the  $M_{\text{BH}}-M_{\text{bulge}}$  relation (see Fig. 4 in Nesvadba et al., 2011). We will therefore refer to this offset as the N11 offset.

### 6.2.2. Eddington ratio

The Eddington ratio represents the rate at which a black hole is accreting compared to the maximal accretion rate considering a spherical accretion (i.e. Eddington limit). This Eddington ratio ( $\lambda$ ) is defined as follows:

$$\lambda = \frac{\kappa_{\text{AGN}}^{\text{Bol}} L_{\text{AGN}}^{\text{IR}}}{L^{\text{Edd}}}, \quad (4)$$

where  $L_{\text{AGN}}^{\text{IR}}$  is in  $L_{\odot}$ ,  $\kappa_{\text{AGN}}^{\text{Bol}}$  is the bolometric correction from IR (set to 6 here, see § 6.1.2, Appendix C and Appendix D) and the Eddington luminosity (the maximal luminosity radiated at given black hole mass),  $L^{\text{Edd}}$ , is defined as:

$$L^{\text{Edd}} = \frac{4\pi G M_{\text{BH}} m_p c}{\sigma_T} = 3.29 \times 10^4 \times M_{\text{BH}}^{\text{Edd}}, \quad (5)$$

where  $m_p$  is the mass of the proton,  $G$  the gravitational constant,  $c$  the speed of light,  $\sigma_T$  the Thomson cross section of the electron,  $L^{\text{Edd}}$  is in  $L_{\odot}$  and  $M_{\text{BH}}^{\text{Edd}}$  in  $M_{\odot}$ . Rearranging Eq. 4 and Eq. 5, one can obtain an estimate of the black hole mass for a given Eddington ratio and IR luminosity. Observations on quasars show a typical Eddington ratio  $\lambda \sim 0.1$  (Kollmeier et al., 2006; Vestergaard & Osmer, 2009; Ballo et al., 2012). We therefore consider an alternate black hole mass defined through Eq. 4 and Eq 5, making use of  $L_{\text{AGN}}^{\text{IR}}$  and setting  $\lambda=0.1$ . We refer

<sup>11</sup> Even in the case of a non-spheroidal geometry, the most important factor appears to be observed the mass of the galaxy, with little evolution with redshift (Jahnke et al., 2009, Appendix D)

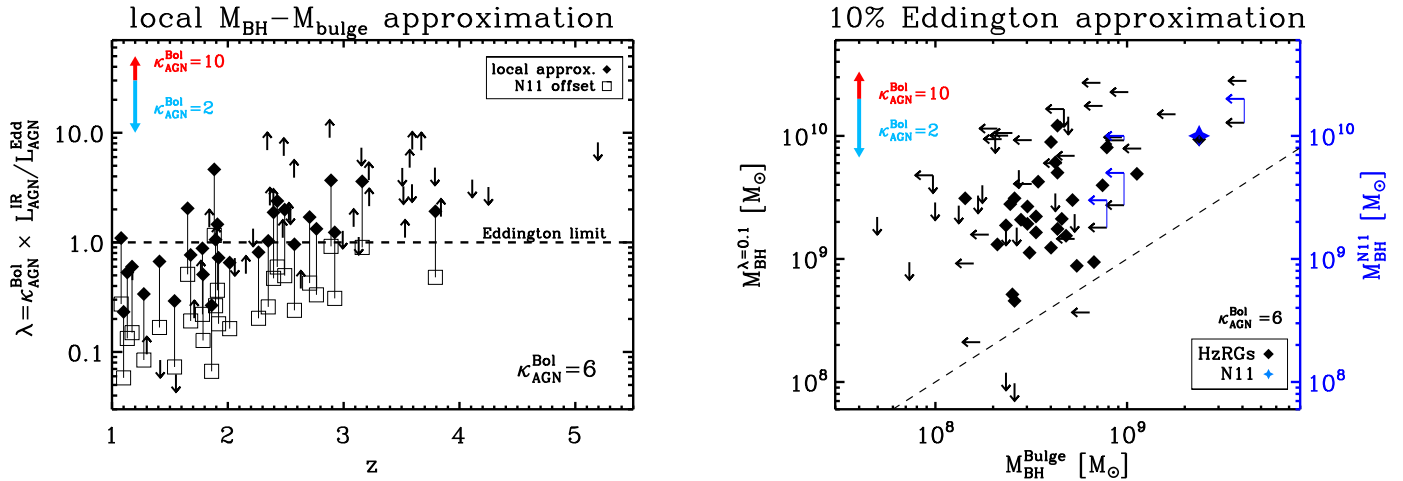


**Fig. 6.** Illustration of the two different, mutually exclusive assumptions (§ 6.2.3). On both figures, we assume  $\kappa_{\text{AGN}}^{\text{Bol}} = 6$ . We also plot the influence of  $\kappa_{\text{AGN}}^{\text{Bol}}$  with a vector of the most likely values (see Appendix C). *Left:* Eddington ratio  $\lambda$  (Eq. 4) versus redshift. We draw the Eddington limit at  $\lambda=1.0$  (dashed line). We assume  $\kappa_{\text{AGN}}^{\text{Bol}} = 6$ . Black diamonds are the calculated Eddington ratios assuming the  $M_{\text{BH}} - M_{\text{Gal}}$  relation while the open squares linked by a thin line represent the same black hole assuming the offset from the local relation from (Nesvadba et al., 2011, see text for details). *Right:*  $M_{\text{BH}}$  from the two different hypothesis, assuming the local  $M_{\text{BH}} - M_{\text{Gal}}$  (bottom axis) and assuming  $\lambda=0.1$  (left axis). The dashed line represent the one-to-one relation. The blue points (arrows and star) are the black hole masses measured from  $H\alpha$  lines (Nesvadba et al., 2011) and compared to the black hole masses from the stellar masses from (De Breuck et al., 2010). These points therefore do not assume the  $\lambda=0.1$ .

to this approximation as the 10% Eddington approximation (see Fig. 6 right, Appendix C and Appendix D for a discussion of the systematic effects).

### 6.2.3. Two hypotheses on Eddington ratio and black hole mass

Figure 6 summarises the two previously introduced methods to estimate  $M_{\text{BH}}$  (with stellar mass, § 6.2.1 the local approximation and Eddington ratio, § 6.2.2, the 10% Eddington approximation).

The left panel presents the Eddington ratios calculated assuming the local  $M_{\text{BH}} - M_{\text{Bulge}}$  relation with black diamonds and with the N11 offset from the same relation from Nesvadba et al. (2011) as empty squares. The latter implies a lower  $\lambda$  as they have a larger black hole mass. We also illustrate the Eddington limit ( $\lambda=1$ ). While  $\lambda$  suggests an increasing trend with redshift (factor of  $\sim 10$  between  $z=1$  and  $z=3$ , with or without the N11 offset), the main difference holds in the range of Eddington ratios. We stress that our uncertainties on  $M_{\text{BH}}$  are still consistent with black holes close to the Eddington limit in both approximations without any need to invoke super Eddington accretion. Anyway, this is interesting as it suggests that to grow rapidly, the SMBH need to accrete close to the Eddington limit to produce their high bolometric luminosities. Moreover, this result seems consistent with quasars, where an increase in  $\lambda$  between  $z=2$  and  $z=6$  has been observed (e.g. Willott et al., 2010; Urrutia et al., 2012).

The right panel presents the two different inferred black hole masses (local and 10% Eddington) plotted against each other. It is clear from this plot that in the case of the 10% Eddington approximation, all black holes appear more massive than suggested by the local  $M_{\text{BH}} - M_{\text{Bulge}}$  relation, i.e. above the dashed line (1:1 relation). As a comparison, we overplot the black hole mass measurements for Nesvadba et al. (2011) scaled from the right axis (in blue). It seems that the 10% Eddington approxi-

mation reproduces well the measured black hole masses from Nesvadba et al. (2011) (within a factor 2).

Independently from these assumptions, we observe here  $M_{\text{BH}} > 10^9 M_{\odot}$  at  $z > 1$ . Optical studies of SDSS quasars (e.g. Vestergaard & Osmer, 2009) show that, though rare,  $> 10^9 M_{\odot}$   $M_{\text{BH}}$  are not exceptional at high redshift. This implies that such extremely massive black holes have acquired most of their mass by  $z=2-4$  as no significantly more massive black holes are found in the local Universe (Kormendy & Ho, 2013, for a recent review). We would therefore be observing the progenitors of the most massive and quiescent black holes at  $z=0$ .

We warn that the last results are degenerate. The only way to overcome this deficiency is through independent measurements of the black hole masses or better constraints on the Eddington ratio ( $\lambda$ ). Constraining the former allows us to bypass the  $M_{\text{BH}} - M_{\text{Bulge}}$  relation, while constraining the latter allows us to estimate the black hole mass without the 10% Eddington approximation ( $\lambda=0.1$ ).

### 6.3. Specific growth properties

Two of the most challenging questions in modern astrophysics are determining the relative growth rate of galaxies and how this growth is related to the growth and activity of their central supermassive black holes. The relative growth of galaxies and their black holes can be specified as the specific star formation rate (sSFR) and the specific black hole accretion rate (s $M_{\text{BH}}$ ). Galaxies at high and low redshift follow a reasonably tight ‘‘main sequence’’ of star formation in the SFR- $M_{\star}$  plane (e.g. Noeske et al., 2007; Elbaz et al., 2007, 2011). How is the relative growth rate of the stellar mass of radio galaxies related to the general population of star forming galaxies? We have already shown that powerful high redshift radio galaxies are forming stars at very high rates but they are also massive. Are their relative growth rates, their sSFR, higher than normal star forming galaxies? Being very luminous AGN, we know their black

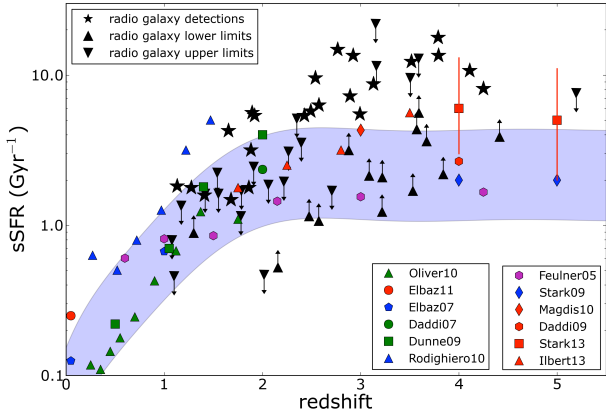


**Fig. 7.** The specific star-formation rate (sSFR, in  $\text{Gyr}^{-1}$ ) as a function of redshift. The various colored points represent measurements from the literature at  $M_{\star} \sim 10^{10} M_{\odot}$ ; see the references in the legend at the bottom right. Since the slope of the sSFR- $M_{\star}$  relation is approximately zero, the rate at which the sSFR evolves is largely independent of  $M_{\star}$ . Thus this is an appropriate comparison, even for galaxies as massive as the radio galaxies studied here. The black stars, triangles, and upside-down triangles represent the radio galaxy detections, lower limits, and upper limits to the sSFR, respectively. The blue shaded region represents the scatter in the observed sSFR values ( $\pm 0.3$  dex). This rendition of the evolution of the sSFR is inspired by a similar plot in Weinmann et al. (2011). See also Lenhert et al., in prep.

hole accretion rates are high, but is the supermassive black hole growing at a relative rate that is consistent with maintaining the relationship of spheroid mass and black hole mass similar to what is observed at low redshift?

### 6.3.1. sSFR of high redshift radio galaxies

The specific star formation rate provides an estimate of the instantaneous relative stellar mass growth rates of galaxies. If galaxies were able to sustain their star formation over a significant time and at the rate observed, the inverse of the sSFR is the mass doubling time scale. Interestingly, the mass doubling time scale is shorter than a Hubble time at all redshifts, becoming comparable to the Hubble time at  $z=0$ . This suggests that if the galaxies have long duty cycles, they can grow their masses relatively quickly at high redshift. Over the redshift range spanned by our radio galaxy sample, the sSFR of the population of star forming galaxies is approximately constant ( $\sim 2 \text{ Gyr}^{-1}$ ) or only slowly increasing with redshift (e.g. Feulner et al., 2005; Rodighiero et al., 2010; Stark et al., 2013; Ilbert et al., 2013).

Compared to the ensemble of distant star forming galaxies, we find that generally the radio galaxies are growing relatively more rapidly (Fig. 7). The combination of upper limits in the *Herschel* photometry and the stellar masses, the number of galaxies with constrained sSFR is only a fraction of the entire sample ( $\sim 30\%$ ). Nevertheless, a significant trend for the sSFRs of the radio galaxies to increase with increasing redshift can be seen. This increase can be characterized as at  $z \lesssim 2.5$ , the sSFR of the radio galaxies is comparable to that of the normal star-forming galaxy population (i.e., no AGN) while at  $z \gtrsim 2.5$ , the radio galaxies lie significantly above (about a factor of 3)

the galaxy population. The scatter for the radio galaxies is a bit higher than in the galaxy population,  $\sim \pm 0.5$  dex compared to  $\sim \pm 0.3$  dex for the non-AGN galaxies. However, given the more limited number of radio galaxies, this difference is not significant. The offset to higher values by a factor  $\sim 3$  for the radio galaxies at  $z \gtrsim 2.5$  is significant. This offset is to be compared to the systematic uncertainties associated with the calculation of the sSFR (see Appendix D). Notably, the uncertainties on the IMF are already taken into account in the blue area (Weinmann et al., 2011). Overall, the results might shift due to systematic uncertainties, but differentially, it is unlikely to wipe out any differences between our sample and the ensemble of galaxies. We also note that radio galaxies are at the bright-end of the K-z diagram (Rocca-Volmerange et al., 2004), and present comparable  $L_{\text{SB}}^{\text{IR}}$  than SMGs (see § 6.1.1), so there are naturally expected to lie in a different area of the SFR- $M_{\star}$  diagram than normal, more quiescent galaxies (e.g. Elbaz et al., 2011).

The cause of the offset at higher redshifts in the sSFR of radio galaxies compared to the normal population of star forming galaxies is not known. Morphological evidence for galaxies lying above the main sequence of star formation suggests that mergers may play a significant role in increasing the sSFR (e.g. De Breuck et al., 2005; Elbaz et al., 2011; Sargent et al., 2013). This picture seems consistent with the trend for radio galaxies to appear in disturbed systems (e.g. Ivison et al., 2008, 2012; Seymour et al., 2012; Wylezalek et al., 2013b). However, whether or not merging is the only cause of perturbed systems is still an open question for the sample of radio galaxies studied here, especially in light of the fact that radio galaxies generally lie in galaxy over-densities (Pascarelle et al., 1996; Venemans et al., 2007; Overzier et al., 2008; Kuiper et al., 2010; Wylezalek et al., 2013a). Galaxies in over densities at high redshift may preferentially have higher sSFRs (Elbaz et al., 2007, Cooke et al., in prep.).

Whatever the cause of their elevated sSFRs, what is clear is that the mass doubling time of the powerful radio galaxy population is short, only about 100 Myr at  $z \gtrsim 2.5$ . If such a relative growth rate could be sustained for 1 Gyr, the typical radio galaxy would have grown by a factor of 1000. Thus despite their high masses, the current star formation rate and relative growth rate do not need to be sustained for a significant fraction of the local Hubble time (1-2 Gyrs over the redshift range spanned in our sample). Notably, the mass depletion time scales are generally very short, of order 100 Myr or less (Ivison et al., 2012; Emonts et al., 2011, 2013). This either suggests that powerful radio galaxies generally represent the last phases of their rapid growth or that, given their relatively rich environments, they are being continuously (re-)fuelled. Their large stellar masses, significantly greater than the fiducial stellar mass turnover in the galaxy co-moving volume density and their overall consistency with the old ages derived for local early type galaxies, suggest these are the almost fully formed progenitors of local early type galaxies (Bernardi et al., 2010). So it may well be that these galaxies are at the end of their formation epoch. They likely formed the bulk of their stars at much higher redshifts, consistent with the stellar synthesis fitting to the broad-band SEDs of a few of these galaxies (Rocca-Volmerange et al., 2013).

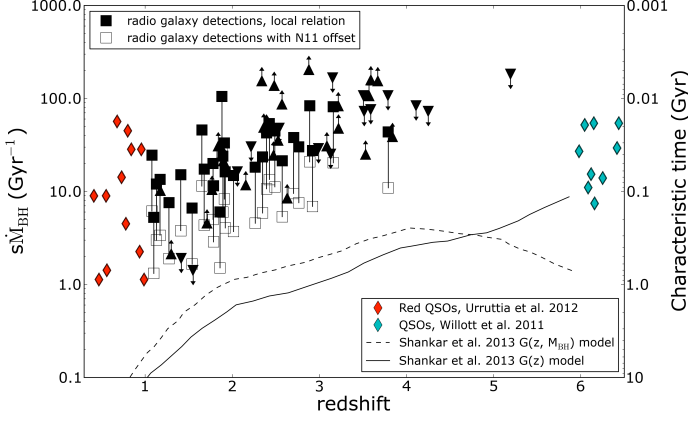


**Fig. 8.**  $s\dot{M}_{\text{BH}}$  versus redshift.  $s\dot{M}_{\text{BH}}$  is reported here with the two assumptions on black hole masses discussed on Fig. 6. The black filled squares are the local  $M_{\text{BH}}-M_{\text{Gal}}$  assumption and the empty square the offset expected from (Nesvadba et al., 2011, see § 6.2.3). We also report other QSO samples for comparison (as indicated in the legend; Willott et al., 2010; Urrutia et al., 2012). In addition, we compare our specific accretion rates with predictions of two models for the growth rate of  $M_{\text{BH}}=10^9 M_{\odot}$  black holes similar to our mass estimates (dashed and solid thick lines, see text for details; Shankar et al., 2013).

### 6.3.2. Specific black hole accretion rate

The specific black hole accretion rate ( $s\dot{M}_{\text{BH}}$ ) corresponds to the inverse of the mass doubling time for the black hole. Following Shankar et al. (2013),  $s\dot{M}_{\text{BH}}$  can be defined as follows:

$$s\dot{M}_{\text{BH}} = 2.5 \times 10^{-9} \frac{\lambda}{f} = \frac{\dot{M}_{\text{BH}}^{\text{acc}}}{M_{\text{BH}}}, \quad (6)$$

where  $\lambda$  is the Eddington ratio (calculated in § 6.2.2), and  $f$  is the actual fraction of mass feeding the black hole and increasing its mass, defined as  $f=\epsilon/(1-\epsilon)$ , where  $\epsilon$  is the radiative efficiency factor (see Eq. 2). Fig. 8 presents a mildly increasing value of  $s\dot{M}_{\text{BH}}$  with redshift, a flattening at  $z=4-5$ , and then a possible decline at  $z>6$ . This behaviour is very similar to what we observed in the  $s\text{SFR}$  (Fig. 8). The characteristic time for the growth of the black hole is  $t_S < 100 \text{ Myr}$  for  $\lambda > 0.5$  and  $\epsilon=0.1$  (see § 6.2.2 and Appendix D for related uncertainties).

How do these estimates compare to other classes of powerful AGN? In order to compare our radio galaxies to similar objects, we also show estimates of  $s\dot{M}_{\text{BH}}$  from various samples of quasars from the literature and we use Eq. 6 in order to calculate  $s\dot{M}_{\text{BH}}$  from the Eddington ratio for these samples. The high redshift sample from Willott et al. (2010) provides the necessary constraints for high redshift optically selected quasars at  $z\sim 6.2$ , while the sample from Urrutia et al. (2012) provides this information for the lower redshift ( $z\sim 0.7$ ) red quasars. Both of these samples of quasars have similar specific accretion rates compared to high redshift radio galaxies under a similar set of assumptions. So high specific accretion rates appear to be a generic feature of bolometrically luminous AGN whether or not they are radio loud.

In addition, Fig. 8 also compares our specific accretion rate estimates with models for the growth of supermassive black holes (Shankar et al., 2013). The models we are specifically comparing to are for the evolution of very massive black holes,

$M_{\text{BH}}=10^9 M_{\odot}$ , similar to what we think are the best mass estimates for the black holes in these radio galaxies (Nesvadba et al., 2011). The models of Shankar et al. (2013) that satisfy the most observational constraints are those that allow the peak of an assumed Gaussian distribution of Eddington accretion rates to evolve with redshift,  $G(z)$ , or with both redshift and black hole mass,  $G(z, M_{\text{BH}})$ . These models for  $M_{\text{BH}}=10^9 M_{\odot}$  fall far below our estimates, by 1-2 orders of magnitude. While these models seek to reproduce the average growth rate of very massive black holes, they fail to reproduce the intense growing phase of the “quasar mode”. However, black holes this massive are rare and do not contribute significantly to the overall growth of black holes at high redshift. However, it is also true that because of their extreme masses lying at the exponential end of the mass function, they provide strong constraints on any model. This is especially true given their potential impact on their host galaxies. Having specific accretion rates off by orders of magnitude means the impact of the AGN on its surroundings, whether it be the surrounding interstellar, intra-cluster, or intergalactic medium, will be greatly underestimated.

### 6.4. Are the SMBHs outgrowing their hosts?

The accretion rate of the BH compared to the SFR (Fig. 3), the relatively high BH accretion rates relative to the Eddington limit (Fig. 6), and  $s\dot{M}_{\text{BH}}$  compared to  $s\text{SFR}$  (Fig. 9) all seem to suggest that the super massive black holes in powerful radio galaxies at high redshift may have out-grown and/or may be out-growing their host galaxies. Whether the black hole is too massive compared to its host, or it is accreting at large Eddington ratio, the black hole of radio galaxies is or will be (in a near future) off the  $M_{\text{BH}}-M_{\text{Bulge}}$  relation. This offset is happening when the black holes are growing very rapidly, with characteristic times of  $< 100 \text{ Myr}$  for doubling their masses. At the same time the stellar mass of the hosts are also growing very rapidly, but apparently not rapidly enough (Fig. 9). Thus to recover the local ratio of black hole and host mass as observed locally, the host of radio galaxies need to “catch up” with their overly massive black holes. We therefore have potential evidence for non-coeval growth of the radio galaxies and their central black holes. In the process, black holes appear to grow first, extremely quickly and efficiently, then the host catch up to fall again the observed local ratio  $M_{\text{BH}}/M_{\text{gal}}$ .

Knowing the duration of the AGN phase would allow to estimate the time lag,  $R_{\text{lag}}$ , which is how long the host galaxy will need to grow at its current rate to get back on the local ratio of stellar to black hole mass. We can calculate this relative time lag assuming a simple model of constant growth or at least a growth rate with a well defined average. Let us define the final mass of the galaxy (or BH) after an episode of growth as a linear equation:

$$M_{\text{gal}}^{\text{final}} = M_{\text{gal}}^{\text{init}} + \dot{M}_{\text{gal}} \Delta T_{\text{gal}}, \quad (7)$$

where  $\Delta T_{\text{gal}}$  is the duration of the star formation (or fueling of the black hole,  $\Delta T_{\text{BH}}$ ),  $\dot{M}_{\text{gal}}$  is the star formation rate (or the mass accretion rate on to the black hole,  $\dot{M}_{\text{BH}}$ ), and the initial,  $M_{\text{gal}}^{\text{init}}$ , and final mass of the galaxy,  $M_{\text{gal}}^{\text{final}}$  (or BH,  $M_{\text{BH}}^{\text{init}}$  and  $M_{\text{BH}}^{\text{final}}$ ). We parameterize the growth of galaxies and black holes in exactly the same linear way. Assuming that the galaxy and the black hole start and end on the ratio of their masses as defined by the local stellar mass of the spheroid mass black hole mass relationship, dividing the two equations allows us to estimate the ratio of the duration of the star formation and the mass accretion onto the

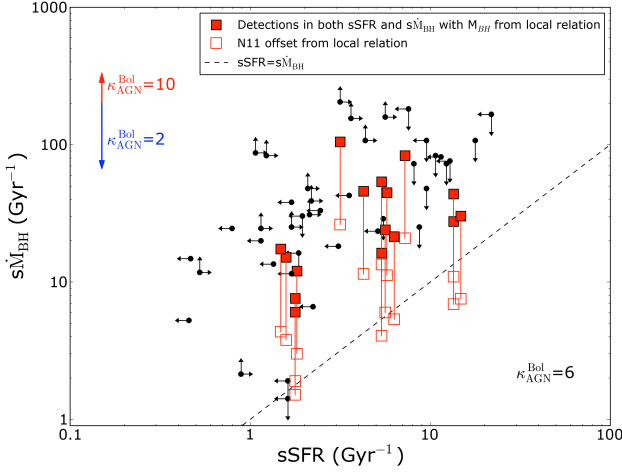


**Fig. 9.** The specific star-formation rate (sSFR, in  $\text{Gyr}^{-1}$ ) versus the specific black hole accretion rate,  $s\dot{M}_{\text{BH}}$  (in  $\text{Gyr}^{-1}$ ). The galaxies with constrained estimates of both sSFR and  $s\dot{M}_{\text{BH}}$  are shown in red, while the arrows indicated upper or lower limits for each or both quantities.  $s\dot{M}_{\text{BH}}$  was estimated using the local  $M_{\text{BH}}-M_{\text{Bulge}}$  relation (filled red diamonds) or using the N11 offset (empty red squares, see § 6.2.3). The dashed line indicates where the  $s\dot{M}_{\text{BH}}=s\text{SFR}$ .

BH that enables the galaxies to have the local  $M_{\text{gal}}/M_{\text{BH}}$  ratio. Dividing these two equations and rearranging the terms gives:

$$R_{\text{lag}} = \frac{\Delta T_{\text{gal}}}{\Delta T_{\text{BH}}} \approx \frac{\dot{M}_{\text{BH}}/M_{\text{BH}}^{\text{init}}}{\dot{M}_{\text{gal}}/M_{\text{gal}}^{\text{init}}} \approx 8. \quad (8)$$

The relative time for the mass of the galaxy to catch up with mass of the black hole such that it falls back onto the local  $M_{\text{BH}}-M_{\text{Bulge}}$  relation,  $R_{\text{lag}}$  is simply the ratio between the  $s\dot{M}_{\text{BH}}$  and sSFR. For our simple model, this means if the black hole growth lasts for 20 Myr, the typical lifetime of a quasar phase (e.g. Steidel et al., 2002; Hopkins et al., 2005), the galaxy will need at least 160 Myr to catch-up with the black hole growth. This is assuming that the actual measured growth rate is the average over the time over which the growth occurred under our given framework, see § 6.1.1–6.3.2. This simplistic model shows that galaxy activity needs to be much longer than the AGN phase in order to catch up after the relative rapid black hole growth. This would naturally explain the observation that the black holes in radio galaxies lie preferentially above the  $M_{\text{BH}}-M_{\text{gal}}$  relation. It may be that already the mass of the BH lies above the relation (Nesvadba et al., 2011) which would then require even more time for the host galaxy to catch up.

### 6.5. The future evolution of powerful radio galaxies

We have found that radio galaxies are growing their stellar populations and supermassive black holes very rapidly. They are able to double their respective masses in a few 100 Myr or less. Interestingly, it appears that, relatively, the supermassive black hole is out-growing or has out-grown its host galaxy. Crudely speaking, the host galaxy will require about an order-of-magnitude longer than the lifetime of the AGN for the host galaxy to catch up. “Catching up” in this context means how much longer will it take for the galaxy at its current sSFR to have

a mass sufficient to land on the local  $M_{\text{BH}}-M_{\text{Bulge}}$  relation once the BH growth has slowed. We propose here to explore different scenarios making use of our previously calculated parameters:

**High redshift powerful radio galaxies will never land on the  $M_{\text{BH}}-M_{\text{Bulge}}$  relation.** In the case of an over-massive black hole (compared to its host),  $R_{\text{lag}}$  indicates that the black hole and its host are not growing at the same rate. The gas supply on larger scales can satisfy the necessary condition to feed simultaneously both the black hole and its host galaxy over the same timescale (though note the severe problems in terms of the physical processes required to bring the gas down to the central engine; Alexander & Hickox, 2012). However, joint feeding implies that radio galaxies might never land on the local  $M_{\text{BH}}-M_{\text{Bulge}}$  relation. In the local Universe only a handful of deviant objects have been observed (e.g. van den Bosch et al., 2012). This scenario is plausible since powerful high redshift radio galaxies are rare objects (only few hundred have been observed out to  $z=5$  so far).

**High redshift powerful radio galaxies will eventually land on the  $M_{\text{BH}}-M_{\text{Bulge}}$  relation.** A variation of the previous scenario can be proposed. Indeed, the galaxies can experience their growth through mergers. Several merging scenarios can be instigated, both major/minor and gas poor/gas rich mergers. Major mergers are rare events but they are expected to be mostly gas rich at high redshift as the gas fraction increases significantly (e.g. Tacconi et al., 2010). Notably, in the case of a major merger, gas can be efficiently brought to the innerpart of the galaxy ( $<1\text{kpc}$ ) and probably feeds the black hole and star formation simultaneously, allowing a new episode of black hole growth. The triggering event of the radio galaxy episode is still an open discussion, but recent studies suggest that major mergers can indeed play an important role (e.g. Ramos Almeida et al., 2013). In the case of minor mergers, gas rich companions could form the stars and be accreted within the cosmic time. This scenario is supported by some observational evidence thanks to high resolution imaging with *HST* (Miley et al., 2006; Seymour et al., 2012). This is also related to the size evolution of galaxies as well as the compactness of early-type galaxies at high redshift (e.g. Daddi et al., 2005; van Dokkum et al., 2008; Delaye et al., 2013), the change in the mass function with cosmic time (Ilbert et al., 2013), the light profiles and elemental abundance ratios in the outer regions of massive ellipticals (Huang et al., 2013; Greene et al., 2013), and the fact that at constant co-moving density, the mass of massive early-type galaxies grew by about a factor of 4 over approximately the last 10 Gyr (e.g. van Dokkum et al., 2010; Ilbert et al., 2013). As HzRGs are sitting in dense environments, probably in the centre of proto-clusters (e.g. Wylezalek et al., 2013a), they are likely to experience an important series of minor dry mergers, consistent with the size evolution scenario. Therefore, high redshift powerful radio galaxies will finally land on the  $M_{\text{BH}}-M_{\text{Bulge}}$  at  $z=0$ .

**High redshift powerful radio galaxies will land on the  $M_{\text{BH}}-M_{\text{Bulge}}$  relation but on a longer timescale.** In the case of black holes starting on the local relation and experiencing a fast, important growth, they will be significantly off the  $M_{\text{BH}}-M_{\text{Bulge}}$  relation in a relatively short timescale ( $\sim 10$  Myr). The host, at the current sSFR, will roughly need 10 times more in order to “catch up” with the black hole. Nevertheless, several observations suggest the contrary. Indeed, to support such a high SFR, an important, continuous supply of gas is required. Such amounts of gas



is presently available in the HzRG systems (e.g. Emonts et al., 2013). Nevertheless, this gas possesses properties which indicate that even if a host growth is possible, it is unlikely to happen in this short timescale. Indeed, HzRGs present copious outflows in ionized and neutral gas (Nesvadba et al., 2006, 2007), gas with substantial angular momentum (van Ojik et al., 1996; Humphrey et al., 2008) or gas in the close environment (Ivison et al., 2012; Emonts et al., 2013). Before participating to the host growth, this gas needs first to be driven into the galaxy. Our best guess is that this gas will actually participate to the host growth, but in a further episode of star formation. The  $R_{\text{lag}}$  is therefore a lower limit of the time lag between the black hole and its host.

**High redshift powerful radio galaxies are examples of a symbiotic growth.** A variation of the previous scenario is by invoking a shorter timescale for the important black hole growth ( $<1$  Myr), the host at the current star formation can “keep up” with its black hole much more easily. Indeed, typical starburst can last for tens of Myrs (e.g. Kennicutt, 1998). Although convenient, this scenario imply that we are looking at the very peak of the AGN activity for all sources and not at the peak of their star formation. If indeed possible, this is unlikely to be the case, (i) given the large scatter seen, for instance, in Fig. 3; and (ii) because the radio selection of our sources which is uncorrelated with the IR luminosity (§ 5.3). Moreover, as mentioned earlier, the variability does induce scatter in our distributions but is not playing a fundamental role on the average.

More observations at high resolution throughout the electromagnetic spectrum, and especially tighter constraints on the BH mass and the mass of the spheroidal component of radio galaxies are needed to test these different scenarios (see § 6.1.1–6.3.2 for our adopted assumptions and Appendix D for a summary of the uncertainties)

## 7. Conclusion

We present new *Herschel* and sub-mm observations for the HeRGÉ sample consisting on 70 powerful radio galaxies spanning  $1 < z < 5.2$ . Complemented by other data sets, we now have continuous coverage of the IR spectral energy distribution over the range from 16-870  $\mu\text{m}$ . All galaxies in our sample have integrated IR luminosities  $L_{\text{IR}} > 10^{12} L_{\odot}$ , classifying them as ULIRGs, while half of all the sources at  $z > 2$  have  $L_{\text{IR}} > 10^{13} L_{\odot}$  and are HyLIRGs.

We use the DecomPIR code to decompose the IR SEDs of galaxies in our sample in a robust and uniform way into an AGN and SB components. To make these fits, we assume a single AGN template and a variety of starburst templates. Our results for the AGN contribution are conservative in that we assumed a single template and it is possible that this template could lead to an underestimate of its contribution to the IR SED. The estimated  $L_{\text{AGN}}^{\text{IR}}$  and  $L_{\text{SB}}^{\text{IR}}$  from our decomposition imply both high black hole mass accretion rates ( $1 M_{\odot} \text{yr}^{-1} < \dot{M}_{\text{BH}} < 100 M_{\odot} \text{yr}^{-1}$ ) and vigorous on-going star formation ( $100 M_{\odot} \text{yr}^{-1} < \text{SFR} < 5000 M_{\odot} \text{yr}^{-1}$ ). Although no strong correlation is detected between these rates, this result implies that both the black hole and its host galaxy are experiencing rapid growth, with the relative growth of the black hole exceeding that of the host galaxy.

Assuming empirical relations and basic physical assumptions, we estimate  $M_{\text{BH}}$  from the stellar masses and infrared AGN luminosities. The black holes appear overly massive

compared to their hosts and are likely accreting close to the Eddington limit ( $\lambda \sim 1$ ), similar to estimates for radio quiet quasars. Alternatively, for lower Eddington rates, the black holes are more massive than predicted by the local  $M_{\text{BH}}-M_{\text{buldge}}$  relationship.

We derive the specific growth properties, both the specific star formation rate, sSFR, and the specific black hole mass accretion rate,  $s\dot{M}_{\text{BH}}$ . Compared to galaxies that lie along the sSFR-stellar mass relation at  $z \geq 2.5$  radio galaxies appear to have higher sSFR. At  $z \lesssim 2.5$ , radio galaxies appear have the same or perhaps lower sSFR generally.

We explore different scenarios for the future growth of radio galaxies. These scenarios are that high redshift powerful radio galaxies (i) will never land on the  $M_{\text{BH}}-M_{\text{Buldge}}$  relation; (ii) will land on the local  $M_{\text{BH}}-M_{\text{Buldge}}$  relation, but at low redshift; (iii) will land on the  $M_{\text{BH}}-M_{\text{Buldge}}$  on a longer timescale than our estimated  $R_{\text{lag}}$ ; or (iv) are indeed experiencing a symbiotic growth. However, observational evidence favours the scenario in which radio galaxies will land again on the  $M_{\text{BH}}-M_{\text{Buldge}}$  relation, but on a long timescale (most probably  $\gg 100$  Myr).

*Acknowledgements.* GD warmly thanks Clive Tadhunter and Rob Ivison for their comments allowing a significative improvement of this paper. GD thanks also the referee for his comments helping to clarify this paper. NS is the recipient of an Australian Research Council Future Fellowship. FEB acknowledges support from Basal-CATA PFB-06/2007 and CONICYT-Chile grants FONDECYT 1101024 and Anillo ACT1101. EI acknowledges funding from CONICYT/FONDECYT postdoctoral project N°:3130504. The work of D.S. was carried out at Jet Propulsion Laboratory, California Institute of Technology, under a contract with NASA. Herschel is an ESA space observatory with science instruments provided by European-led Principal Investigator consortia and with important participation from NASA. This work is based in part on observations made with the *Spitzer Space Telescope*. This work is based on observations made with the APEX Telescope, based on the Chajnantor Plateau in Chile. HIPE is a joint development by the Herschel Science Ground Segment Consortium, consisting of ESA, the NASA Herschel Science Center, and the HIFI, PACS, and SPIRE consortia. *Facilities:* *Spitzer, Herschel, APEX*

## References

- Aird, J., Nandra, K., Laird, E. S., et al. 2010, MNRAS, 401, 2531  
 Alexander, D. M. & Hickox, R. C. 2012, New A Rev., 56, 93  
 Alexander, D. M., Smail, I., Bauer, F. E., et al. 2005, Nature, 434, 738  
 Antonucci, R. 2011, ArXiv e-prints  
 Archibald, E. N., Dunlop, J. S., Hughes, D. H., et al. 2001, MNRAS, 323, 417  
 Asmus, D., Gandhi, P., Smette, A., Höning, S. F., & Duschl, W. J. 2011, A&A, 536, A36  
 Ballo, L., Heras, F. J. H., Barcons, X., & Carrera, F. J. 2012, A&A, 545, A66  
 Barger, A. J., Cowie, L. L., Sanders, D. B., et al. 1998, Nature, 394, 248  
 Barthel, P., Haas, M., Leipski, C., & Wilkes, B. 2012, ApJ, 757, L26  
 Barthel, P. D. 1989, ApJ, 336, 606  
 Bernardi, M., Shankar, F., Hyde, J. B., et al. 2010, MNRAS, 404, 2087  
 Blain, A. W., Smail, I., Ivison, R. J., & Kneib, J.-P. 1999, MNRAS, 302, 632  
 Blundell, K. M., Rawlings, S., Eales, S. A., Taylor, G. B., & Bradley, A. D. 1998, MNRAS, 295, 265  
 Blundell, K. M., Rawlings, S., & Willott, C. J. 1999, AJ, 117, 677  
 Bongiorno, A., Merloni, A., Brusa, M., et al. 2012, MNRAS, 427, 3103  
 Bornancini, C. G., O’Mill, A. L., Gurovich, S., & Lambas, D. G. 2010, MNRAS, 406, 197  
 Calzetti, D. 2012, ArXiv e-prints  
 Cao, X. & Li, F. 2008, MNRAS, 390, 561  
 Carilli, C. L., Harris, D. E., Pentericci, L., et al. 2002, ApJ, 567, 781  
 Carilli, C. L., Roettgering, H. J. A., van Ojik, R., Miley, G. K., & van Breugel, W. J. M. 1997, ApJS, 109, 1  
 Chapman, S. C., Blain, A. W., Smail, I., & Ivison, R. J. 2005, ApJ, 622, 772  
 Chen, C.-T. J., Hickox, R. C., Alberts, S., et al. 2013, ApJ, 773, 3  
 Cimatti, A., di Serego Alighieri, S., Vernet, J., Cohen, M., & Fosbury, R. A. E. 1998, ApJ, 499, L21  
 Cleary, K., Lawrence, C. R., Marshall, J. A., Hao, L., & Meier, D. 2007, ApJ, 660, 117  
 Crocker, A. F., Bureau, M., Young, L. M., & Combes, F. 2011, MNRAS, 410, 1197  
 Daddi, E., Dickinson, M., Morrison, G., et al. 2007, ApJ, 670, 156

- Daddi, E., Renzini, A., Pirkhal, N., et al. 2005, *ApJ*, 626, 680
- Dale, D. A., Helou, G., Magdis, G. E., et al. 2014, *ApJ*, 784, 83
- Davis, S. W. & Laor, A. 2011, *ApJ*, 728, 98
- De Breuck, C., Downes, D., Neri, R., et al. 2005, *A&A*, 430, L1
- De Breuck, C., Seymour, N., Stern, D., et al. 2010, *ApJ*, 725, 36
- De Breuck, C., van Breugel, W., Stanford, S. A., et al. 2002, *AJ*, 123, 637
- Del Moro, A., Alexander, D. M., Mullaney, J. R., et al. 2013, *A&A*, 549, A59
- Delaye, L., Huertas-Company, M., Mei, S., et al. 2013, *ArXiv e-prints*
- Dey, A., van Breugel, W., Vacca, W. D., & Antonucci, R. 1997, *ApJ*, 490, 698
- Dicken, D., Tadhunter, C., Axon, D., et al. 2009, *ApJ*, 694, 268
- Dicken, D., Tadhunter, C., Axon, D., et al. 2012, *ApJ*, 745, 172
- Dicken, D., Tadhunter, C., Axon, D., et al. 2010, *ApJ*, 722, 1333
- Diolaiti, E., Bendinelli, O., Bonaccini, D., et al. 2000, *A&AS*, 147, 335
- Draine, B. T. 2003, *ARA&A*, 41, 241
- Drouart, G., De Breuck, C., Vernet, J., et al. 2012, *A&A*, 548, A45
- Elbaz, D., Daddi, E., Le Borgne, D., et al. 2007, *A&A*, 468, 33
- Elbaz, D., Dickinson, M., Hwang, H. S., et al. 2011, *A&A*, 533, A119
- Elvis, M., Wilkes, B. J., McDowell, J. C., et al. 1994, *ApJS*, 95, 1
- Emonts, B. H. C., Feain, I., Mao, M. Y., et al. 2011, *ApJ*, 734, L25
- Emonts, B. H. C., Feain, I., Röttgering, H. J. A., et al. 2013, *MNRAS*, 430, 3465
- Engel, H., Tacconi, L. J., Davies, R. I., et al. 2010, *ApJ*, 724, 233
- Esquej, P., Alonso-Herrero, A., González-Martín, O., et al. 2014, *ApJ*, 780, 86
- Falder, J. T., Stevens, J. A., Jarvis, M. J., et al. 2010, *MNRAS*, 405, 347
- Feltre, A., Hatziminaoglou, E., Hernán-Caballero, A., et al. 2013, *MNRAS*, 434, 2426
- Ferrarese, L. & Merritt, D. 2000, *ApJ*, 539, L9
- Feulner, G., Gabasch, A., Salvato, M., et al. 2005, *ApJ*, 633, L9
- Fioc, M. & Rocca-Volmerange, B. 1997, *A&A*, 326, 950
- Fitzpatrick, E. L. 1999, *PASP*, 111, 63
- Fritz, J., Franceschini, A., & Hatziminaoglou, E. 2006, *MNRAS*, 366, 767
- Galametz, A., Stern, D., De Breuck, C., et al. 2012, *ApJ*, 749, 169
- Gebhardt, K., Bender, R., Bower, G., et al. 2000, *ApJ*, 539, L13
- Greene, J. E., Murphy, J. D., Graves, G. J., et al. 2013, *ArXiv e-prints*
- Griffin, M. J., Abergel, A., Abreu, A., et al. 2010, *A&A*, 518, L3
- Haas, M., Klaas, U., Müller, S. A. H., et al. 2003, *A&A*, 402, 87
- Hainline, L. J., Blain, A. W., Smail, I., et al. 2011, *ApJ*, 740, 96
- Hao, C.-N., Xia, X.-Y., Shu-DeMao, Deng, Z.-G., & Wu, H. 2008, *Chinese J. Astron. Astrophys.*, 8, 12
- Hao, H., Elvis, M., Civano, F., et al. 2014, *MNRAS*, 438, 1288
- Hardcastle, M. J., Evans, D. A., & Croston, J. H. 2007, *MNRAS*, 376, 1849
- Hardcastle, M. J. & Worrall, D. M. 1999, *MNRAS*, 309, 969
- Häring, N. & Rix, H.-W. 2004, *ApJ*, 604, L89
- Harrison, C. M., Alexander, D. M., Mullaney, J. R., et al. 2012, *ApJ*, 760, L15
- Hatch, N. A., De Breuck, C., Galametz, A., et al. 2011, *MNRAS*, 410, 1537
- Hatch, N. A., Overzier, R. A., Röttgering, H. J. A., Kurk, J. D., & Miley, G. K. 2008, *MNRAS*, 383, 931
- Hatch, N. A., Röttgering, H. J. A., Miley, G. K., et al. 2013, *MNRAS*, 436, 2244
- Hatziminaoglou, E., Omont, A., Stevens, J. A., et al. 2010, *A&A*, 518, L33
- Hickox, R. C., Mullaney, J. R., Alexander, D. M., et al. 2013, *ArXiv e-prints*
- Hickox, R. C., Myers, A. D., Brodwin, M., et al. 2011, *ApJ*, 731, 117
- Hicks, E. K. S., Davies, R. I., Malkan, M. A., et al. 2009, *ApJ*, 696, 448
- Hodge, J. A., Karim, A., Smail, I., et al. 2013, *ApJ*, 768, 91
- Hopkins, A. M. & Beacom, J. F. 2006, *ApJ*, 651, 142
- Hopkins, P. F., Hernquist, L., Cox, T. J., et al. 2006, *ApJS*, 163, 1
- Hopkins, P. F., Hernquist, L., Martini, P., et al. 2005, *ApJ*, 625, L71
- Hopkins, P. F. & Quataert, E. 2010, *MNRAS*, 407, 1529
- Huang, S., Ho, L. C., Peng, C. Y., Li, Z.-Y., & Barth, A. J. 2013, *ApJ*, 768, L28
- Hughes, D. H., Serjeant, S., Dunlop, J., et al. 1998, *Nature*, 394, 241
- Humphrey, A., Villar-Martín, M., Vernet, J., et al. 2008, *MNRAS*, 383, 11
- Ilbert, O., McCracken, H. J., Le Fèvre, O., et al. 2013, *A&A*, 556, A55
- Iverson, R. J., Morrison, G. E., Biggs, A. D., et al. 2008, *MNRAS*, 390, 1117
- Iverson, R. J., Smail, I., Amblard, A., et al. 2012, *MNRAS*, 425, 1320
- Jahnke, K., Bongiorno, A., Brusa, M., et al. 2009, *ApJ*, 706, L215
- Janssen, R. M. J., Röttgering, H. J. A., Best, P. N., & Brinchmann, J. 2012, *A&A*, 541, A62
- Jogee, S., Scoville, N., & Kenney, J. D. P. 2005, *ApJ*, 630, 837
- Kaiser, C. R., Dennett-Thorpe, J., & Alexander, P. 1997, *MNRAS*, 292, 723
- Karim, A., Swinbank, A. M., Hodge, J. A., et al. 2013, *MNRAS*, 432, 2
- Kartaltepe, J. S., Sanders, D. B., Le Floch, E., et al. 2010, *ApJ*, 709, 572
- Kennicutt, Jr., R. C. 1998, *ARA&A*, 36, 189
- Ker, L. M., Best, P. N., Rigby, E. E., Röttgering, H. J. A., & Gendre, M. A. 2012, *MNRAS*, 420, 2644
- Klamer, I. J., Ekers, R. D., Bryant, J. J., et al. 2006, *MNRAS*, 371, 852
- Kollmeier, J. A., Onken, C. A., Kochanek, C. S., et al. 2006, *ApJ*, 648, 128
- Kormendy, J. & Ho, L. C. 2013, *ARA&A*, 51, 511
- Kovács, A. 2008, in *Society of Photo-Optical Instrumentation Engineers (SPIE) Conference Series*, Vol. 7020, *Society of Photo-Optical Instrumentation Engineers (SPIE) Conference Series*
- Krawczyk, C. M., Richards, G. T., Mehta, S. S., et al. 2013, *ApJS*, 206, 4
- Krolik, J. H. 1999, *Active galactic nuclei : from the central black hole to the galactic environment*
- Kuiper, E., Hatch, N. A., Röttgering, H. J. A., et al. 2010, *MNRAS*, 405, 969
- Kuiper, E., Hatch, N. A., Venemans, B. P., et al. 2011, *MNRAS*, 417, 1088
- Labbé, I., Huang, J., Franx, M., et al. 2005, *ApJ*, 624, L81
- Lauer, T. R., Faber, S. M., Richstone, D., et al. 2007, *ApJ*, 662, 808
- Lehnert, M. D. & Heckman, T. M. 1996, *ApJ*, 472, 546
- Leipski, C., Haas, M., Willner, S. P., et al. 2010, *ApJ*, 717, 766
- Leipski, C., Meisenheimer, K., Walter, F., et al. 2013, *ApJ*, 772, 103
- Leipski, C., Meisenheimer, K., Walter, F., et al. 2014, *ArXiv e-prints*
- Magdis, G. E., Elbaz, D., Dickinson, M., et al. 2011, *A&A*, 534, A15
- Magorrian, J., Tremaine, S., Richstone, D., et al. 1998, *AJ*, 115, 2285
- Marchesini, D., van Dokkum, P. G., Förster Schreiber, N. M., et al. 2009, *ApJ*, 701, 1765
- Marconi, A., Risaliti, G., Gilli, R., et al. 2004, *MNRAS*, 351, 169
- Martínez-Sansigre, A. & Rawlings, S. 2011, *MNRAS*, 414, 1937
- Matthews, T. A., Morgan, W. W., & Schmidt, M. 1964, *ApJ*, 140, 35
- Merloni, A., Bongiorno, A., Bolzonella, M., et al. 2010, *ApJ*, 708, 137
- Merloni, A., Rudnick, G., & Di Matteo, T. 2004, *MNRAS*, 354, L37
- Michalowski, M. J., Dunlop, J. S., Cirasuolo, M., et al. 2012, *A&A*, 541, A85
- Miley, G. & De Breuck, C. 2008, *A&A Rev.*, 15, 67
- Miley, G. K., Overzier, R. A., Zirm, A. W., et al. 2006, *ApJ*, 650, L29
- Mullaney, J. R., Alexander, D. M., Goulding, A. D., & Hickox, R. C. 2011, *MNRAS*, 414, 1082
- Nenkova, M., Sirocky, M. M., Ivezić, Ž., & Elitzur, M. 2008, *ApJ*, 685, 147
- Nesvadba, N. P. H., De Breuck, C., Lehnert, M. D., et al. 2011, *A&A*, 525, A43
- Nesvadba, N. P. H., Lehnert, M. D., De Breuck, C., Gilbert, A., & van Breugel, W. 2007, *A&A*, 475, 145
- Nesvadba, N. P. H., Lehnert, M. D., De Breuck, C., Gilbert, A. M., & van Breugel, W. 2008, *A&A*, 491, 407
- Nesvadba, N. P. H., Lehnert, M. D., Eisenhauer, F., et al. 2006, *ApJ*, 650, 693
- Netzer, H. 2009, *MNRAS*, 399, 1907
- Nguyen, H. T., Schulz, B., Levenson, L., et al. 2010, *A&A*, 518, L5
- Noeske, K. G., Weiner, B. J., Faber, S. M., et al. 2007, *ApJ*, 660, L43
- Ogle, P., Whysong, D., & Antonucci, R. 2006, *ApJ*, 647, 161
- Ott, S. 2010, in *Astronomical Society of the Pacific Conference Series*, Vol. 434, *Astronomical Data Analysis Software and Systems XIX*, ed. Y. Mizumoto, K.-I. Morita, & M. Ohishi, 139
- Overzier, R. A., Bouwens, R. J., Cross, N. J. G., et al. 2008, *ApJ*, 673, 143
- Pascarelle, S. M., Windhorst, R. A., Driver, S. P., Ostrander, E. J., & Keel, W. C. 1996, *ApJ*, 456, L21
- Pearson, C., Lim, T., North, C., et al. 2013, *Experimental Astronomy*
- Pentericci, L., McCarthy, P. J., Röttgering, H. J. A., et al. 2001, *ApJS*, 135, 63
- Pentericci, L., Röttgering, H. J. A., Miley, G. K., et al. 1999, *A&A*, 341, 329
- Pentericci, L., Van Reeve, W., Carilli, C. L., Röttgering, H. J. A., & Miley, G. K. 2000, *A&AS*, 145, 121
- Pier, E. A. & Krolik, J. H. 1993, *ApJ*, 418, 673
- Pilbratt, G. L., Riedinger, J. R., Passvogel, T., et al. 2010, *A&A*, 518, L1
- Poglitich, A., Waelkens, C., Geis, N., et al. 2010, *A&A*, 518, L2
- Popesso, P., Magnelli, B., Buttiglione, S., et al. 2012, *ArXiv e-prints*
- Ramos Almeida, C., Bessiere, P. S., Tadhunter, C. N., et al. 2013, *MNRAS*, 436, 997
- Rawlings, J. I., Seymour, N., Page, M. J., et al. 2013, *MNRAS*, 429, 744
- Reuland, M., Röttgering, H., van Breugel, W., & De Breuck, C. 2004, *MNRAS*, 353, 377
- Reuland, M., van Breugel, W., Röttgering, H., et al. 2003, *ApJ*, 592, 755
- Richards, G. T., Lacy, M., Storrie-Lombardi, L. J., et al. 2006, *ApJS*, 166, 470
- Rocca-Volmerange, B., Drouart, G., De Breuck, C., et al. 2013, *MNRAS*, 429, 2780
- Rocca-Volmerange, B., Le Borgne, D., De Breuck, C., Fioc, M., & Moy, E. 2004, *A&A*, 415, 931
- Rodighiero, G., Vaccari, M., Franceschini, A., et al. 2010, *A&A*, 515, A8
- Rosario, D. J., Burtscher, L., Davies, R., et al. 2013, *ApJ*, 778, 94
- Rosario, D. J., Santini, P., Lutz, D., et al. 2012, *A&A*, 545, A45
- Roseboom, I. G., Oliver, S. J., Kunz, M., et al. 2010, *MNRAS*, 409, 48
- Sargent, M. T., Daddi, E., Béthermin, M., et al. 2013, *ArXiv e-prints*
- Schuller, F. 2012, in *Society of Photo-Optical Instrumentation Engineers (SPIE) Conference Series*, Vol. 8452, *Society of Photo-Optical Instrumentation Engineers (SPIE) Conference Series*
- Scott, A. E. & Stewart, G. C. 2014, *MNRAS*, 438, 2253
- Seymour, N., Altieri, B., De Breuck, C., et al. 2012, *ApJ*, 755, 146
- Seymour, N., Ogle, P., De Breuck, C., et al. 2008, *ApJ*, 681, L1
- Seymour, N., Stern, D., De Breuck, C., et al. 2007, *ApJS*, 171, 353
- Shankar, F., Weinberg, D. H., & Miralda-Escudé, J. 2013, *MNRAS*, 428, 421
- Shankar, F., Weinberg, D. H., & Shen, Y. 2010, *MNRAS*, 406, 1959
- Shen, Y., Strauss, M. A., Oguri, M., et al. 2007, *AJ*, 133, 2222
- Simpson, J., Swinbank, M., Smail, I., et al. 2013, *ArXiv e-prints*

- Somerville, R. S., Primack, J. R., & Faber, S. M. 2001, *MNRAS*, 320, 504
- Stark, D. P., Schenker, M. A., Ellis, R., et al. 2013, *ApJ*, 763, 129
- Steidel, C. C., Hunt, M. P., Shapley, A. E., et al. 2002, *ApJ*, 576, 653
- Stevens, J. A., Ivison, R. J., Dunlop, J. S., et al. 2003, *Nature*, 425, 264
- Swinbank, M., Simpson, J., Smail, I., et al. 2013, *ArXiv e-prints*
- Symeonidis, M., Vaccari, M., Berta, S., et al. 2013, *MNRAS*
- Tacconi, L. J., Genzel, R., Neri, R., et al. 2010, *Nature*, 463, 781
- Tacconi, L. J., Genzel, R., Smail, I., et al. 2008, *ApJ*, 680, 246
- Thomas, D., Maraston, C., Bender, R., & Mendes de Oliveira, C. 2005, *ApJ*, 621, 673
- Urrutia, T., Lacy, M., Spoon, H., et al. 2012, *ApJ*, 757, 125
- van Breugel, W. J. M., Stanford, S. A., Spinrad, H., Stern, D., & Graham, J. R. 1998, *ApJ*, 502, 614
- van den Bosch, R. C. E., Gebhardt, K., Gültekin, K., et al. 2012, *Nature*, 491, 729
- van Dokkum, P. G., Franx, M., Kriek, M., et al. 2008, *ApJ*, 677, L5
- van Dokkum, P. G., Whitaker, K. E., Brammer, G., et al. 2010, *ApJ*, 709, 1018
- van Ojik, R., Roettgering, H. J. A., Carilli, C. L., et al. 1996, *A&A*, 313, 25
- Venemans, B. P., Röttgering, H. J. A., Miley, G. K., et al. 2007, *A&A*, 461, 823
- Vernet, J., Fosbury, R. A. E., Villar-Martín, M., et al. 2001, *A&A*, 366, 7
- Vestergaard, M. & Osmer, P. S. 2009, *ApJ*, 699, 800
- Videla, L., Lira, P., Andrews, H., et al. 2013, *ApJS*, 204, 23
- Volonteri, M., Sikora, M., & Lasota, J.-P. 2007, *ApJ*, 667, 704
- Wang, R., Wagg, J., Carilli, C. L., et al. 2011, *AJ*, 142, 101
- Wang, S. X., Brandt, W. N., Luo, B., et al. 2013, *ApJ*, 778, 179
- Wardlow, J. L., Smail, I., Coppin, K. E. K., et al. 2011, *MNRAS*, 415, 1479
- Weinmann, S. M., Neistein, E., & Dekel, A. 2011, *MNRAS*, 417, 2737
- Weiß, A., Kovács, A., Coppin, K., et al. 2009, *ApJ*, 707, 1201
- Willott, C. J., Albert, L., Arzoumanian, D., et al. 2010, *AJ*, 140, 546
- Willott, C. J., Omont, A., & Bergeron, J. 2013, *ApJ*, 770, 13
- Wylezalek, D., Galametz, A., Stern, D., et al. 2013a, *ApJ*, 769, 79
- Wylezalek, D., Vernet, J., De Breuck, C., et al. 2013b, *MNRAS*, 428, 3206
- Young, L. M., Bureau, M., Davis, T. A., et al. 2011, *MNRAS*, 414, 940
- Zhang, X., Lu, Y., & Yu, Q. 2012, *ApJ*, 761, 5
- Zirm, A. W., Dickinson, M., & Dey, A. 2003, *ApJ*, 585, 90

**Table 2.** *Herschel* observations. All are part of the OT1 seymour 1 program except when specified.

| Name           | RA (J2000) | Dec (J2000) | $z$   | ObsID PACS 1 | ObsID PACS 2 | ObsID SPIRE | Notes           |
|----------------|------------|-------------|-------|--------------|--------------|-------------|-----------------|
| 6C 0032+412    | 00:34:53.1 | +41:31:31.5 | 3.670 | 1342237860   | 1342237861   | 1342238254  |                 |
| MRC 0037-258   | 00:39:56.4 | -25:34:31.0 | 1.100 | 1342235414   | 1342235415   | 1342221924  |                 |
| 6CE 0058+495   | 01:01:18.8 | +49:50:12.3 | 1.173 | 1342237864   | 1342237865   | 1342238256  |                 |
| MRC 0114-211   | 01:16:51.4 | -20:52:06.7 | 1.410 | 1342224381   | 1342224382   | 1342234710  |                 |
| TN J0121+1320  | 01:21:42.7 | +13:20:58.0 | 3.516 | 1342238029   | 1342238030   | 1342223211  |                 |
| 6CE 0132+330   | 01:35:30.4 | +33:16:59.6 | 1.710 | 1342237844   | 1342237845   | 1342237505  |                 |
| 6C 0140+326    | 01:43:43.8 | +32:53:49.3 | 4.413 | 1342214047   | 1342214048   | 1342213490  | KPGT kmeisenh 1 |
| MRC 0152-209   | 01:54:55.8 | -20:40:26.3 | 1.920 | 1342238786   | 1342238787   | 1342234712  |                 |
| MRC 0156-252   | 01:58:33.4 | -24:59:31.7 | 2.016 | 1342238739   | 1342238740   | 1342234716  |                 |
| TN J0205+2242  | 02:05:10.7 | +22:42:50.4 | 3.506 | 1342237400   | 1342237401   | 1342237501  |                 |
| MRC 0211-256   | 02:13:30.5 | -25:25:20.6 | 1.300 | 1342239459   | 1342239460   | 1342234717  |                 |
| TXS 0211-122   | 02:14:17.4 | -11:58:46.0 | 2.340 | 1342238111   | 1342238112   | 1342237532  |                 |
| 3C 65          | 02:23:43.5 | +40:00:52.7 | 1.176 | 1342238005   | 1342238006   | 1342239821  |                 |
| MRC 0251-273   | 02:53:16.7 | -27:09:11.6 | 3.160 | 1342237410   | 1342237411   | 1342214558  |                 |
| MRC 0316-257   | 03:18:12.1 | -25:35:09.7 | 3.130 | 1342239422   | 1342239423   | 1342214555  |                 |
| MRC 0324-228   | 03:27:04.5 | -22:39:42.1 | 1.894 | 1342239424   | 1342239425   | 1342238288  |                 |
| MRC 0350-279   | 03:52:51.6 | -27:49:22.6 | 1.900 | 1342239418   | 1342239419   | 1342227718  |                 |
| MRC 0406-244   | 04:08:51.5 | -24:18:16.4 | 2.427 | 1342225214   | 1342225215   | 1342239859  |                 |
| 4C 60.07       | 05:12:55.1 | +60:30:51.0 | 3.788 | 1342206050   | 1342206051   | 1342203606  | KPGT kmeisenh 1 |
| PKS 0529-549   | 05:30:25.4 | -54:54:23.2 | 2.575 | 1342236654   | 1342236655   | 1342226641  |                 |
| WN J0617+5012  | 06:17:39.3 | +50:12:54.2 | 3.153 | 1342242754   | 1342242755   | 1342229114  |                 |
| 4C 41.17       | 06:50:52.2 | +41:30:30.1 | 3.792 | 1342206336   | 1342206337   | 1342204958  | KPGT kmeisenh 1 |
| WN J0747+3654  | 07:47:29.4 | +36:54:38.1 | 2.992 | 1342229038   | 1342229039   | 1342229478  |                 |
| 6CE 0820+3642  | 08:23:48.1 | +36:32:46.4 | 1.860 | 1342243302   | 1342243303   | 1342230755  |                 |
| 5C 7.269       | 08:28:38.8 | +25:28:27.1 | 2.218 | 1342232224   | 1342232225   | 1342230774  |                 |
| USS 0828+193   | 08:30:53.4 | +19:13:16.2 | 2.572 | 1342232222   | 1342232223   | 1342230772  |                 |
| 6CE 0901+3551  | 09:04:32.3 | +35:39:04.1 | 1.910 | 1342232232   | 1342232233   | 1342230750  |                 |
| B2 0902+34     | 09:05:30.1 | +34:07:56.0 | 3.395 | 1342232230   | 1342232231   | 1342230737  |                 |
| 6CE 0905+3955  | 09:08:16.9 | +39:43:26.0 | 1.883 | 1342232236   | 1342232237   | 1342230748  |                 |
| TN J0924-2201  | 09:24:19.9 | -22:01:42.3 | 5.195 | 1342198543   | 1342198544   | 1342198865  | KPGT kmeisenh 1 |
| 6C 0930+389    | 09:33:06.9 | +38:41:50.1 | 2.395 | 1342232036   | 1342232037   | 1342230738  |                 |
| USS 0943-242   | 09:45:32.7 | -24:28:49.7 | 2.923 | 1342233248   | 1342233249   | 1342234835  |                 |
| 3C 239         | 10:11:45.4 | +46:28:19.8 | 1.781 | 1342231241   | 1342231242   | 1342230739  |                 |
| MG 1019+0534   | 10:19:33.4 | +05:34:34.8 | 2.765 | 1342233228   | 1342233229   | 1342222672  |                 |
| MRC 1017-220   | 10:19:49.0 | -22:19:59.6 | 1.768 | 1342233103   | 1342233104   | 1342234838  |                 |
| WN J1115+5016  | 11:15:06.9 | +50:16:23.9 | 2.540 | 1342231395   | 1342231396   | 1342222662  |                 |
| 3C 257         | 11:23:09.4 | +05:30:17.1 | 2.474 | 1342221966   | 1342221967   | 1342210514  | GT1 pbarthel 1  |
| WN J1123+3141  | 11:23:55.7 | +31:41:26.7 | 3.217 | 1342222681   | 1342222682   | 1342222669  |                 |
| PKS 1138-262   | 11:40:48.4 | -26:29:08.8 | 2.156 | 1342222456   | 1342222457   | 1342210877  | GT1 baltieri 3  |
| 3C 266         | 11:45:43.6 | +49:46:05.2 | 1.275 | 1342222695   | 1342222696   | 1342222663  |                 |
| 6C 1232+39     | 12:35:04.7 | +39:25:38.9 | 3.220 | 1342234365   | 1342234366   | 1342232703  |                 |
| USS 1243+036   | 12:45:38.4 | +03:23:20.7 | 3.570 | 1342223828   | 1342223829   | 1342224982  |                 |
| TN J1338-1942  | 13:38:26.1 | -19:42:30.7 | 4.110 | 1342237906   | 1342237907   | 1342226186  |                 |
| 4C 24.28       | 13:48:14.9 | +24:15:50.5 | 2.879 | 1342233533   | 1342233534   | 1342234787  |                 |
| 3C 294         | 14:06:53.2 | +34:11:21.1 | 1.786 | 1342233525   | 1342233526   | 1342236145  |                 |
| USS 1410-001   | 14:13:15.1 | -00:22:59.7 | 2.363 | 1342237900   | 1342237901   | 1342236162  |                 |
| 8C 1435+635    | 14:36:37.2 | +63:19:14.4 | 4.250 | 1342209329   | 1342209330   | 1342199362  | KPGT kmeisenh 1 |
| USS 1558-003   | 16:01:17.3 | -00:28:46.2 | 2.527 | 1342238057   | 1342238058   | 1342238311  |                 |
| USS 1707+105   | 17:10:06.9 | +10:31:10.2 | 2.349 | 1342230116   | 1342230117   | 1342229578  |                 |
| LBDS 53W002    | 17:14:14.8 | +50:15:30.6 | 2.393 | 1342234084   | 1342234085   | 1342229153  |                 |
| LBDS 53W069    | 17:20:02.5 | +49:44:51.0 | 1.432 | 1342231668   | 1342231669   | 1342229155  |                 |
| LBDS 53W091    | 17:22:32.9 | +50:06:01.3 | 1.552 | 1342234086   | 1342234087   | 1342229156  |                 |
| 3C 356.0       | 17:24:19.3 | +50:57:36.2 | 1.079 | 1342219036   | 1342219037   | 1342206197  | GT1 pbarthel 1  |
| 7C 1751+6809   | 17:50:50.0 | +68:08:26.4 | 1.540 | 1342233557   | 1342233558   | 1342223224  |                 |
| 7C 1756+6520   | 17:57:05.4 | +65:19:53.1 | 1.416 | 1342233561   | 1342233562   | 1342229141  |                 |
| 3C 368         | 18:05:06.4 | +11:01:33.1 | 1.132 | 1342216599   | 1342216600   | 1342216954  | GT1 pbarthel 1  |
| 7C 1805+6332   | 18:05:56.8 | +63:33:13.1 | 1.840 | 1342233563   | 1342233564   | 1342229140  |                 |
| 4C 40.36       | 18:10:55.7 | +40:45:24.0 | 2.265 | 1342225262   | 1342225263   | 1342229165  |                 |
| TXS J1908+7220 | 19:08:23.7 | +72:20:11.8 | 3.530 | 1342232248   | 1342232249   | 1342220624  |                 |
| WN J1911+6342  | 19:11:49.6 | +63:42:09.6 | 3.590 | 1342233575   | 1342233576   | 1342220864  |                 |
| TN J2007-1316  | 20:07:53.3 | -13:16:43.6 | 3.840 | 1342217425   | 1342217426   | 1342230833  |                 |
| MRC 2025-218   | 20:27:59.5 | -21:40:56.9 | 2.630 | 1342217421   | 1342217422   | 1342230830  |                 |
| MRC 2048-272   | 20:51:03.6 | -27:03:02.5 | 2.060 | 1342218548   | 1342218549   | 1342218982  |                 |
| MRC 2104-242   | 21:06:58.3 | -24:05:09.1 | 2.491 | 1342232504   | 1342232505   | 1342218979  |                 |
| 4C 23.56       | 21:07:14.8 | +23:31:45.0 | 2.483 | 1342222551   | 1342222552   | 1342233325  |                 |
| MG 2144+1928   | 21:44:07.6 | +19:29:14.6 | 3.592 | 1342235313   | 1342235314   | 1342220527  |                 |
| USS 2202+128   | 22:05:14.2 | +13:05:33.0 | 2.706 | 1342235311   | 1342235312   | 1342220528  |                 |
| MRC 2224-273   | 22:27:43.3 | -27:05:01.7 | 1.679 | 1342234103   | 1342234104   | 1342234742  |                 |
| B3 J2330+3927  | 23:30:24.8 | +39:27:12.5 | 3.086 | 1342225457   | 1342225458   | 1342234918  |                 |
| 4C 28.58       | 23:51:59.2 | +29:10:29.0 | 2.891 | 1342225467   | 1342225468   | 1342234922  |                 |
| 3C 470         | 23:58:36.0 | +44:04:46.0 | 1.653 | 1342237858   | 1342237859   | 1342236248  |                 |

**Table 3.** *Herschel* photometry. Values between parenthesis are the *signal-to-noise* estimates from the images *before* including the uncertainties in the flux calibration. Values between square brackets are weak detections ( $2\sigma < F^{\text{gal}} < 3\sigma$ ). Upper limits are given at the  $3\sigma$  level of the noise (see § 2.2.3 for how these were determined). Flux given in *italic* were deconvolved using *Starfinder* (See § 2.2.2).

| Name           | PACS (70 $\mu\text{m}$ )<br>[mJy] | PACS (100 $\mu\text{m}$ )<br>[mJy] | PACS (160 $\mu\text{m}$ )<br>[mJy] | SPIRE (250 $\mu\text{m}$ )<br>[mJy] | SPIRE (350 $\mu\text{m}$ )<br>[mJy] | SPIRE (500 $\mu\text{m}$ )<br>[mJy] |
|----------------|-----------------------------------|------------------------------------|------------------------------------|-------------------------------------|-------------------------------------|-------------------------------------|
| 6C 0032+412    | ...                               | < 11.2                             | < 21.3                             | < 14.2                              | < 15.4                              | < 20.2                              |
| MRC 0037-258   | < 7.5                             | ...                                | < 28.0                             | < 14.6                              | < 16.6                              | < 18.9                              |
| 6CE 0058+495   | < 9.2                             | ...                                | < 35.5                             | < 19.2                              | < 19.8                              | < 29.1                              |
| MRC 0114-211   | [5.5± 2.7( 2.0)]                  | ...                                | 32.2± 9.4( 3.5)                    | 24.3± 7.5( 3.3)                     | < 36.2                              | < 30.8                              |
| TN J0121+1320  | ...                               | < 7.9                              | < 24.2                             | 15.9± 5.7( 2.8)]                    | [18.0± 6.6( 2.8)]                   | < 18.4                              |
| 6CE 0132+330   | < 10.2                            | ...                                | < 26.0                             | < 14.3                              | < 16.7                              | < 19.5                              |
| 6C 0140+326    | < 6.9                             | ...                                | < 19.8                             | < 14.7                              | < 14.5                              | < 16.5                              |
| MRC 0152-209   | 22.6± 3.5( 6.8)                   | ...                                | 119.2± 9.8(15.4)                   | 105.0± 8.6(23.0)                    | 81.3± 7.3(17.6)                     | 64.4± 6.8(12.6)                     |
| MRC 0156-252   | ...                               | 13.8± 3.7( 3.8)                    | < 23.3                             | < 15.0                              | < 18.0                              | < 20.9                              |
| TN J0205+2242  | ...                               | < 7.3                              | < 30.2                             | < 14.6                              | < 14.7                              | < 17.7                              |
| MRC 0211-256   | < 9.5                             | ...                                | [ 17.4± 6.6( 2.6)]                 | 25.0± 3.8( 7.3)                     | 25.9± 5.8( 4.7)                     | [15.7± 5.9( 2.7)]                   |
| TXS 0211-122   | ...                               | [7.4± 3.4( 2.2)]                   | [11.7± 5.9( 2.0)]                  | < 15.9                              | < 19.2                              | < 24.5                              |
| 3C 65          | < 10.5                            | ...                                | < 16.1                             | < 15.9                              | < 17.7                              | < 21.9                              |
| MRC 0251-273   | ...                               | < 10.0                             | < 18.7                             | < 15.7                              | < 14.1                              | < 19.5                              |
| MRC 0316-257   | ...                               | < 11.1                             | [ 17.7± 7.2( 2.5)]                 | 22.7± 5.1( 4.7)                     | 20.2± 5.4( 3.9)                     | < 19.3                              |
| MRC 0324-228   | < 9.1                             | ...                                | 27.9± 5.4( 5.4)                    | 61.8± 6.7(12.1)                     | 35.5± 5.9( 6.7)                     | [ 17.5± 7.4( 2.4)]                  |
| MRC 0350-279   | < 11.3                            | ...                                | < 25.5                             | < 14.2                              | < 14.0                              | < 15.9                              |
| MRC 0406-244   | ...                               | < 12.3                             | [ 21.5± 7.9( 2.7)]                 | 47.6± 5.6(10.6)                     | 38.7± 5.3( 8.4)                     | 22.8± 5.9( 4.0)                     |
| 4C 60.07       | < 4.9                             | ...                                | < 29.1                             | 46.4± 6.5( 8.2)                     | 49.5± 8.4( 6.5)                     | 48.0± 8.3( 6.3)                     |
| PKS 0529-549   | ...                               | [8.3± 4.0( 2.1)]                   | 31.9± 9.0( 3.6)                    | 35.1± 7.3( 5.1)                     | 43.8± 8.3( 5.6)                     | 40.0± 8.9( 4.8)                     |
| WN J0617+5012  | ...                               | < 7.9                              | < 23.2                             | < 19.3                              | < 21.4                              | < 22.4                              |
| 4C 41.17       | < 4.2                             | ...                                | [ 17.9± 6.8( 2.6)]                 | 28.2± 4.8( 6.5)                     | 35.7± 5.8( 6.8)                     | 31.1± 6.1( 5.5)                     |
| WN J0747+3654  | ...                               | < 8.8                              | < 26.7                             | < 14.9                              | < 18.1                              | < 17.1                              |
| 6CE 0820+3642  | < 11.3                            | ...                                | < 22.5                             | 32.2± 5.1( 7.0)                     | [11.3± 4.7( 2.5)]                   | < 15.4                              |
| 5C 7.269       | ...                               | < 7.8                              | < 25.0                             | < 13.4                              | < 18.0                              | < 14.5                              |
| USS 0828+193   | ...                               | 18.5± 3.5( 5.4)                    | [ 24.0± 9.6( 2.5)]                 | 20.2± 4.5( 4.7)                     | 17.5± 4.7( 3.8)                     | < 17.2                              |
| 6CE 0901+3551  | < 8.6                             | ...                                | < 26.8                             | < 13.8                              | < 16.2                              | < 19.3                              |
| B2 0902+34     | ...                               | < 9.7                              | < 20.9                             | [12.4± 4.6( 2.7)]                   | < 15.3                              | < 15.4                              |
| 6CE 0905+3955  | 34.2± 2.8(15.4)                   | ...                                | 59.8± 11.2( 5.5)                   | 38.8± 4.9( 9.5)                     | 30.9± 5.4( 6.2)                     | < 16.0                              |
| TN J0924-2201  | < 4.6                             | ...                                | < 16.3                             | < 11.4                              | < 16.1                              | < 14.3                              |
| 6C 0930+389    | ...                               | < 9.4                              | < 18.6                             | < 16.7                              | < 15.5                              | < 16.8                              |
| USS 0943-242   | ...                               | < 27.6                             | 23.6± 7.7( 3.1)                    | 25.7± 5.2( 5.2)                     | 31.7± 5.5( 6.3)                     | 35.2± 7.3( 5.1)                     |
| 3C 239         | < 12.7                            | ...                                | < 33.3                             | < 15.5                              | < 15.2                              | < 18.4                              |
| MG 1019+0534   | ...                               | 15.4± 2.9( 5.5)                    | 23.5± 5.8( 4.2)                    | 28.6± 5.4( 5.7)                     | 29.9± 5.3( 6.2)                     | 33.2± 5.3( 7.1)                     |
| MRC 1017-220   | < 7.7                             | ...                                | < 25.1                             | < 17.4                              | < 23.6                              | < 22.4                              |
| WN J1115+5016  | ...                               | < 9.3                              | < 20.7                             | < 17.4                              | < 18.7                              | < 21.4                              |
| 3C 257         | 7.7± 1.5( 5.4)                    | ...                                | [ 14.6± 6.1( 2.4)]                 | 29.8± 4.8( 6.9)                     | 25.6± 4.6( 6.1)                     | 17.4± 5.3( 3.3)                     |
| WN J1123+3141  | ...                               | [ 15.6± 6.2( 2.5)]                 | < 27.2                             | 21.0± 4.6( 4.9)                     | 15.8± 4.6( 3.5)                     | < 19.1                              |
| PKS 1138-262   | ...                               | 25.2± 2.2(13.9)                    | 40.2± 10.2( 4.0)                   | 40.4± 5.9( 7.8)                     | 33.0± 6.1( 5.8)                     | 28.9± 6.7( 4.5)                     |
| 3C 266         | < 9.4                             | ...                                | 28.7± 7.6( 3.8)                    | 14.7± 4.3( 3.5)                     | < 17.8                              | < 20.2                              |
| 6C 1232+39     | ...                               | < 6.7                              | < 26.4                             | < 13.3                              | < 14.0                              | < 17.1                              |
| USS 1243+036   | ...                               | [ 8.3± 3.1( 2.7)]                  | [ 14.1± 6.3( 2.2)]                 | 16.6± 5.6( 3.0)                     | < 19.6                              | < 22.2                              |
| TN J1338-1942  | ...                               | < 5.9                              | < 27.1                             | < 16.6                              | < 17.5                              | < 18.0                              |
| 4C 24.28       | ...                               | 14.2± 3.3( 4.4)                    | 23.3± 7.9( 3.0)                    | < 15.9                              | < 14.6                              | < 14.6                              |
| 3C 294         | < 7.1                             | ...                                | < 27.0                             | < 15.6                              | < 17.9                              | < 20.4                              |
| USS 1410-001   | ...                               | < 10.1                             | < 19.2                             | < 15.0                              | < 17.3                              | < 21.8                              |
| 8C 1435+635    | < 5.2                             | ...                                | < 16.2                             | < 10.4                              | < 11.4                              | < 13.5                              |
| USS 1558-003   | ...                               | < 7.4                              | < 22.4                             | < 16.4                              | < 18.8                              | < 21.0                              |
| USS 1707+105   | ...                               | < 8.6                              | < 27.7                             | < 16.8                              | < 14.9                              | < 19.5                              |
| LBDS 53W002    | ...                               | < 9.4                              | < 24.9                             | < 15.0                              | < 14.3                              | < 16.5                              |
| LBDS 53W069    | < 7.9                             | ...                                | < 24.3                             | < 14.8                              | < 12.8                              | < 17.2                              |
| LBDS 53W091    | < 10.5                            | ...                                | < 36.7                             | < 14.7                              | < 15.2                              | < 17.9                              |
| 3C 356.0       | < 11.8                            | ...                                | < 23.8                             | < 14.1                              | < 14.3                              | < 15.6                              |
| 7C 1751+6809   | < 9.9                             | ...                                | < 26.1                             | < 15.2                              | < 13.9                              | < 15.4                              |
| 7C 1756+6520   | < 8.2                             | ...                                | < 29.8                             | < 14.6                              | < 19.3                              | < 19.5                              |
| 3C 368         | 32.3± 3.5(10.4)                   | ...                                | 52.9± 9.1( 6.1)                    | 35.6± 6.2( 6.3)                     | 19.6± 6.5( 3.1)                     | < 19.0                              |
| 7C 1805+6332   | < 7.4                             | ...                                | < 28.4                             | < 14.6                              | < 17.6                              | < 18.3                              |
| 4C 40.36       | ...                               | < 8.6                              | < 29.3                             | < 16.0                              | < 18.5                              | < 15.6                              |
| TXS J1908+7220 | ...                               | 19.4± 3.1( 6.5)                    | 36.7± 8.1( 4.7)                    | 38.9± 8.0( 5.2)                     | 52.9± 7.7( 7.9)                     | 49.5± 8.6( 6.3)                     |
| WN J1911+6342  | ...                               | 9.2± 3.0( 3.1)                     | < 20.4                             | < 9.4                               | < 15.2                              | < 11.7                              |
| TN J2007-1316  | ...                               | < 7.7                              | < 20.8                             | 16.7± 5.2( 3.3)                     | 16.8± 5.1( 3.4)                     | < 18.9                              |
| MRC 2025-218   | ...                               | < 11.1                             | < 30.7                             | < 18.5                              | < 28.4                              | < 19.5                              |
| MRC 2048-272   | ...                               | < 8.5                              | < 25.3                             | < 15.3                              | < 16.0                              | < 18.6                              |
| MRC 2104-242   | ...                               | 14.4± 3.5( 4.3)                    | [ 22.0± 8.4( 2.6)]                 | [14.2± 5.1( 2.8)]                   | 21.1± 6.6( 3.3)                     | < 15.8                              |
| 4C 23.56       | ...                               | 29.2± 3.2(10.3)                    | [ 17.2± 6.8( 2.6)]                 | < 18.5                              | < 24.2                              | < 25.9                              |
| MG 2144+1928   | ...                               | < 46.1                             | < 40.4                             | < 14.8                              | < 18.1                              | < 17.5                              |
| USS 2202+128   | ...                               | [ 7.2± 2.9( 2.5)]                  | 18.2± 5.7( 3.2)                    | < 13.7                              | < 12.6                              | < 17.1                              |
| MRC 2224-273   | < 10.5                            | ...                                | < 28.2                             | 14.6± 4.8( 3.1)                     | < 17.7                              | < 18.3                              |
| B3 J2330+3927  | ...                               | 9.5± 2.6( 3.8)                     | < 32.2                             | 39.0± 5.8( 7.7)                     | 48.0± 6.4( 8.8)                     | 50.3± 7.5( 7.6)                     |
| 4C 28.58       | ...                               | 22.8± 2.9( 8.6)                    | [ 23.6± 8.7( 2.7)]                 | 42.5± 4.9(11.0)                     | 29.7± 5.4( 6.0)                     | 15.5± 4.5( 3.5)                     |
| 3C 470         | 21.6± 3.7( 6.0)                   | ...                                | 22.5± 7.2( 3.2)                    | 39.2± 5.7( 7.9)                     | 33.5± 6.0( 6.1)                     | 24.9± 6.3( 4.1)                     |

**Table 4.** Sub-mm flux at  $870\ \mu\text{m}$  with LABOCA in this paper, at  $850\ \mu\text{m}$  for all the rest. Flux in square brackets symbolise the weak detection ( $2\sigma < F^{\text{gal}} < 3\sigma$ ). For a description of the observing mode, *WOO* or *mapping* see S 2.4.

| Name           | Flux [mJy] | Obs. mode | References              |
|----------------|------------|-----------|-------------------------|
| 6C 0032+412    | [2.6±1.2]  | -         | Archibald et al. (2001) |
| MRC 0037-258   | <12.9      | WOO       | this paper              |
| 6CE 0058+495   | ...        | -         | -                       |
| MRC 0114-211   | <16.8      | mapping   | this paper              |
| TN J0121+1320  | 7.5±1.0    | -         | Reuland et al. (2004)   |
| 6CE 0132+330   | ...        | -         | -                       |
| 6C 0140+326    | [3.3±1.5]  | -         | Archibald et al. (2001) |
| MRC 0152-209   | 14.5±3.3   | WOO       | this paper              |
| MRC 0156-252   | <21.0      | mapping   | this paper              |
| TN J0205+2242  | <5.2       | -         | Reuland et al. (2004)   |
| MRC 0211-256   | <26.1      | mapping   | this paper              |
| TXS 0211-122   | <24.6      | mapping   | this paper              |
| 3C 65          | ...        | -         | -                       |
| MRC 0251-273   | <8.9       | -         | Reuland et al. (2004)   |
| MRC 0316-257   | <8.8       | -         | Reuland et al. (2004)   |
| MRC 0324-228   | <9.0       | WOO       | this paper              |
| MRC 0350-279   | <23.1      | mapping   | this paper              |
| MRC 0406-244   | <17.8      | WOO       | this paper              |
| 4C 60.07       | 17.1±1.3   | -         | Archibald et al. (2001) |
| PKS 0529-549   | ...        | -         | -                       |
| WN J0617+5012  | <3.2       | -         | Reuland et al. (2004)   |
| 4C 41.17       | 12.1±0.9   | -         | Archibald et al. (2001) |
| WN J0747+3654  | 4.8±1.1    | -         | Reuland et al. (2004)   |
| 6CE 0820+3642  | [2.1±1.0]  | -         | Archibald et al. (2001) |
| 5C 7.269       | <4.7       | -         | Archibald et al. (2001) |
| USS 0828+193   | ...        | -         | -                       |
| 6CE 0901+3551  | <3.45      | -         | Archibald et al. (2001) |
| B2 0902+34     | [2.8±1.0]  | -         | Archibald et al. (2001) |
| 6CE 0905+3955  | 3.6±0.9    | -         | Archibald et al. (2001) |
| TN J0924-2201  | <3.2       | -         | Reuland et al. (2004)   |
| 6C 0930+389    | <3.4       | -         | Archibald et al. (2001) |
| USS 0943-242   | <24.0      | mapping   | this paper              |
| 3C 239         | <3.8       | -         | Archibald et al. (2001) |
| MG 1019+0534   | [2.4±0.9]  | -         | Archibald et al. (2001) |
| MRC 1017-220   | <18.6      | WOO       | this paper              |
| WN J1115+5016  | [3.0±1.3]  | -         | Reuland et al. (2004)   |
| 3C 257         | 5.4±1.0    | -         | Archibald et al. (2001) |
| WN J1123+3141  | 4.9±1.2    | -         | Reuland et al. (2004)   |
| PKS 1138-262   | 12.8±3.3   | -         | Reuland et al. (2004)   |
| 3C 266         | <4.4       | -         | Archibald et al. (2001) |
| 6C 1232+39     | 3.9±0.7    | -         | Archibald et al. (2001) |
| USS 1243+036   | [2.3±1.1]  | -         | Archibald et al. (2001) |
| TN J1338-1942  | 6.9±1.1    | -         | Reuland et al. (2004)   |
| 4C 24.28       | [2.6±1.2]  | -         | Archibald et al. (2001) |
| 3C 294         | <2.5       | -         | Archibald et al. (2001) |
| USS 1410-001   | <10.8      | WOO       | this paper              |
| 8C 1435+635    | 7.8±0.8    | -         | Archibald et al. (2001) |
| USS 1558-003   | <9.6       | WOO       | this paper              |
| USS 1707+105   | <9.3       | WOO       | this paper              |
| LBDS 53W002    | <4.3       | -         | Archibald et al. (2001) |
| LBDS 53W069    | <3.1       | -         | Archibald et al. (2001) |
| LBDS 53W091    | ...        | -         | -                       |
| 3C 356.0       | <4.8       | -         | Archibald et al. (2001) |
| 7C 1751+6809   | ...        | -         | -                       |
| 7C 1756+6520   | ...        | -         | -                       |
| 3C 368         | 4.1±1.1    | -         | Archibald et al. (2001) |
| 7C 1805+6332   | ...        | -         | -                       |
| 4C 40.36       | <3.9       | -         | Archibald et al. (2001) |
| TXS J1908+7220 | 10.8±1.2   | -         | Reuland et al. (2004)   |
| WN J1911+6342  | <11.9      | -         | Reuland et al. (2004)   |
| TN J2007-1316  | 5.8±1.5    | -         | Reuland et al. (2004)   |
| MRC 2025-218   | <10.5      | WOO       | this paper              |
| MRC 2048-272   | <21.0      | mapping   | this paper              |
| MRC 2104-242   | ...        | -         | -                       |
| 4C 23.56       | <4.7       | -         | Archibald et al. (2001) |
| MG 2144+1928   | [2.3±0.9]  | -         | Reuland et al. (2004)   |
| USS 2202+128   | <11.1      | mapping   | this paper              |
| MRC 2224-273   | <12.3      | mapping   | this paper              |
| B3 J2330+3927  | 14.1±1.7   | -         | Reuland et al. (2004)   |
| 4C 28.58       | 3.9±1.2    | -         | Archibald et al. (2001) |
| 3C 470         | 5.6±1.1    | -         | Archibald et al. (2001) |

**Table 6.** Main results from the SED fitting. (\*)See Appendix A. SB template refers to the best-fit template (§ 4.1).  $L_{\text{tot}}^{\text{IR}}$  is the total integrated luminosity (§ 3.1).  $L_{\text{AGN}}^{\text{IR}}, L_{\text{SB}}^{\text{IR}}$  are the integrated AGN and SB luminosity in the 8-1000  $\mu\text{m}$  restframe (§ 5.2).  $f_{\text{AGN}}^{10\mu\text{m}}, f_{\text{AGN}}^{50\mu\text{m}}$  and  $f_{\text{AGN}}^{100\mu\text{m}}$  are the ratio  $S_{\text{AGN}}/S_{\text{SB}}$  at 10, 50 and 100  $\mu\text{m}$  restframe, respectively (§ 4.4 and Appendix B).

| Name           | class | Detect. | SB template | $L_{\text{tot}}^{\text{IR}} [10^{12} L_{\odot}]$ | $L_{\text{AGN}}^{\text{IR}} [10^{12} L_{\odot}]$ | $L_{\text{SB}}^{\text{IR}} [10^{12} L_{\odot}]$ | $f_{\text{AGN}}^{10\mu\text{m}}$ | $f_{\text{AGN}}^{50\mu\text{m}}$ | $f_{\text{AGN}}^{100\mu\text{m}}$ |
|----------------|-------|---------|-------------|--|--|---|----------------------------------|----------------------------------|-----------------------------------|
| 6C 0032+412    | WCD   | 3       | SB2         | 12.2   | 9.6± 1.8   | 3.2± 1.4  | 17.5                             | 1.56                             | 0.350                             |
| MRC 0037-258   | WD    | 2       | SB2         | < 1.5  | 0.9± 0.2   | < 1.0   | > 4.8                            | > 0.4                            | > 0.09                            |
| 6CE 0058+495   | WD    | 2       | SB2         | < 2.2  | 1.0± 0.2   | < 1.4   | > 4.0                            | > 0.3                            | > 0.07                            |
| MRC 0114-211   | WCD   | 5       | SB6         | 3.8  | 1.6± 0.4   | 2.3± 0.6  | 3.8                              | 0.25                             | 0.080                             |
| TN J0121+1320  | CD    | 2       | SB2         | < 9.8  | < 3.0  | 7.5± 0.9  | < 2.2                            | < 0.2                            | < 0.04                            |
| 6CE 0132+330   | WD    | 1       | SB3         | < 1.2  | 0.2± 0.0   | < 1.7   | > 1.0                            | > 0.0                            | > 0.01                            |
| 6C 0140+326    | CD    | 1       | SB6         | < 19.2   | < 15.0   | 6.0± 2.7  | < 13.4                           | < 0.8                            | < 0.28                            |
| MRC 0152-209   | WCD   | 8       | SB2         | 22.3   | 4.5± 1.2   | 17.8± 0.9                                       | 1.4                              | 0.12                             | 0.028                             |
| MRC 0156-252   | WD    | 2       | SB2         | < 8.9  | 8.5± 1.6   | < 3.0   | > 15.4                           | > 1.3                            | > 0.30                            |
| TN J0205+2242  | UL    | 0       | SB2         | < 5.9  | < 2.6  | < 3.7   | ...                              | ...                              | ...                               |
| MRC 0211-256   | WCD   | 6       | SB3         | 2.1  | 0.3± 0.1   | 1.8± 0.2  | 1.7                              | 0.09                             | 0.017                             |
| TXS 0211-122   | WD    | 4       | SB2         | < 9.3  | 9.1± 1.7   | < 4.4   | > 11.4                           | > 1.0                            | > 0.22                            |
| 3C 65          | WD    | 2       | SB2         | < 2.2  | 1.3± 0.2   | < 1.2   | > 6.1                            | > 0.5                            | > 0.12                            |
| MRC 0251-273   | WD    | 2       | SB2         | < 7.6  | 2.8± 0.5   | < 6.1   | > 2.5                            | > 0.2                            | > 0.05                            |
| MRC 0316-257   | CD    | 3       | SB6         | < 8.0  | < 1.6  | 7.9± 1.3  | < 1.1                            | < 0.0                            | < 0.02                            |
| MRC 0324-228   | WCD   | 6       | SB4         | 7.5  | 1.7± 0.6   | 5.8± 0.5  | 1.1                              | 0.18                             | 0.023                             |
| MRC 0350-279   | WD    | 2       | SB2         | < 1.4  | 0.8± 0.1   | < 2.7   | > 1.7                            | > 0.1                            | > 0.03                            |
| MRC 0406-244   | WCD   | 6       | SB4         | 13.0   | 5.5± 1.3   | 7.5± 0.7  | 2.7                              | 0.45                             | 0.057                             |
| 4C 60.07       | CD    | 4       | SB6         | < 32.6   | < 13.0   | 28.8± 1.7                                       | < 2.4                            | < 0.1                            | < 0.05                            |
| PKS 0529-549   | WCD   | 7       | SB3         | 13.2   | 2.7± 0.7   | 10.5± 1.2                                       | 2.4                              | 0.13                             | 0.023                             |
| WN J0617+5012  | UL    | 0       | SB6         | < 5.6  | < 2.0  | < 4.5   | ...                              | ...                              | ...                               |
| 4C 41.17*      | WCD   | 7       | SB6         | 24.0   | 4.6± 1.8   | 19.4± 1.2                                       | 1.3                              | 0.08                             | 0.027                             |
| WN J0747+3654  | CD    | 1       | SB2         | < 5.3  | < 1.6  | 4.5± 1.0  | < 2.0                            | < 0.1                            | < 0.04                            |
| 6CE 0820+3642  | WCD   | 5       | SB2         | 4.0  | 0.8± 0.3   | 3.1± 0.5  | 1.4                              | 0.12                             | 0.028                             |
| 5C 7.269       | UL    | 0       | SB3         | < 5.2  | < 3.1  | < 2.7   | ...                              | ...                              | ...                               |
| USS 0828+193   | WCD   | 6       | SB3         | 18.4   | 15.9± 2.3  | 2.5± 1.0  | 59.0                             | 3.19                             | 0.575                             |
| 6CE 0901+3551  | WD    | 2       | SB2         | < 4.4  | 2.4± 0.4   | < 2.5   | > 5.3                            | > 0.4                            | > 0.10                            |
| B2 0902+34*    | UL    | 4       | SB6         | < 8.4  | < 4.3  | < 5.4   | ...                              | ...                              | ...                               |
| 6CE 0905+3955  | WCD   | 7       | SB2         | 15.5   | 11.0± 1.0  | 4.5± 0.5  | 13.4                             | 1.19                             | 0.268                             |
| TN J0924-2201  | UL    | 0       | SB6         | < 13.5   | < 9.2  | < 5.5   | ...                              | ...                              | ...                               |
| 6C 0930+389    | WD    | 1       | SB2         | < 4.6  | 2.5± 0.6   | < 3.1   | > 4.5                            | > 0.4                            | > 0.09                            |
| USS 0943-242   | WCD   | 6       | SB1         | 14.9   | 1.9± 0.7   | 13.0± 1.5                                       | 0.6                              | 0.08                             | 0.017                             |
| 3C 239         | WD    | 2       | SB2         | < 5.5  | 3.6± 0.6   | < 2.7   | > 7.5                            | > 0.6                            | > 0.15                            |
| MG 1019+0534   | WCD   | 8       | SB1         | 13.8   | 1.7± 0.6   | 12.1± 1.1                                       | 0.6                              | 0.08                             | 0.016                             |
| MRC 1017-220   | WD    | 2       | SB2         | < 4.1  | 2.5± 0.4   | < 2.7   | > 5.0                            | > 0.4                            | > 0.10                            |
| WN J1115+5016  | CD    | 1       | SB2         | < 2.8  | < 0.9  | 2.8± 1.2  | < 1.7                            | < 0.1                            | < 0.03                            |
| 3C 257         | WCD   | 8       | SB4         | 11.2   | 7.2± 1.1   | 4.0± 0.5  | 6.4                              | 1.08                             | 0.136                             |
| WN J1123+3141  | WCD   | 5       | SB2         | 24.4   | 20.6± 3.3  | 3.8± 1.0  | 30.0                             | 2.68                             | 0.600                             |
| PKS 1138-262   | WCD   | 8       | SB3         | 17.2   | 11.6± 1.3  | 5.6± 0.7  | 19.0                             | 1.03                             | 0.185                             |
| 3C 266         | WCD   | 4       | SB6         | 2.0  | 0.5± 0.2   | 1.6± 0.3  | 1.6                              | 0.11                             | 0.034                             |
| 6C 1232+39     | WCD   | 3       | SB2         | 9.2  | 6.2± 1.1   | 3.6± 0.7  | 9.3                              | 0.83                             | 0.186                             |
| USS 1243+036   | WCD   | 5       | SB6         | 13.1   | 8.4± 1.9   | 4.7± 1.7  | 9.5                              | 0.63                             | 0.203                             |
| TN J1338-1942  | CD    | 1       | SB2         | < 9.7  | < 3.6  | 6.8± 1.1  | < 2.9                            | < 0.2                            | < 0.05                            |
| 4C 24.28       | WCD   | 5       | SB2         | 12.8   | 10.4± 1.5  | 2.4± 1.1  | 23.9                             | 2.13                             | 0.478                             |
| 3C 294         | WD    | 2       | SB2         | < 2.1  | 1.1± 0.2   | < 2.2   | > 2.8                            | > 0.2                            | > 0.05                            |
| USS 1410-001   | WD    | 2       | SB2         | < 10.0   | 5.4± 1.0   | < 10.5  | > 2.9                            | > 0.2                            | > 0.05                            |
| 8C 1435+635    | CD    | 1       | SB2         | < 11.6   | < 4.8  | 7.7± 0.8  | < 3.4                            | < 0.3                            | < 0.06                            |
| USS 1558-003   | WD    | 2       | SB5         | < 9.2  | 8.4± 1.5   | < 2.5   | > 10.4                           | > 2.8                            | > 0.24                            |
| USS 1707+105   | WD    | 1       | SB2         | < 3.7  | 1.2± 0.3   | < 3.9   | > 1.7                            | > 0.1                            | > 0.03                            |
| LBDS 53W002    | WD    | 2       | SB2         | < 5.7  | 3.7± 0.7   | < 4.0   | > 5.1                            | > 0.4                            | > 0.10                            |
| LBDS 53W091    | UL    | 0       | SB3         | < 0.9  | < 0.1  | < 1.5   | ...                              | ...                              | ...                               |
| 3C 356.0       | WD    | 2       | SB2         | < 2.6  | 2.0± 0.4   | < 0.9   | > 12.2                           | > 1.0                            | > 0.24                            |
| 7C 1751+6809   | WD    | 2       | SB2         | < 2.0  | 0.4± 0.1   | < 2.0   | > 1.1                            | > 0.1                            | > 0.02                            |
| 7C 1756+6520   | UL    | 0       | SB3         | < 1.2  | < 0.1  | < 1.3   | ...                              | ...                              | ...                               |
| 3C 368         | WCD   | 7       | SB2         | 4.2  | 1.4± 0.3   | 2.8± 0.3  | 2.7                              | 0.24                             | 0.055                             |
| 7C 1805+6332   | WD    | 2       | SB2         | < 3.0  | 1.4± 0.3   | < 2.5   | > 3.2                            | > 0.2                            | > 0.06                            |
| 4C 40.36       | WD    | 1       | SB2         | < 3.9  | 1.5± 0.4   | < 3.5   | > 2.3                            | > 0.2                            | > 0.04                            |
| TXS J1908+7220 | WCD   | 7       | SB6         | 43.7   | 25.4± 3.6  | 18.3± 1.8                                       | 7.4                              | 0.49                             | 0.158                             |
| WN J1911+6342  | UL    | 0       | SB2         | < 7.6  | < 2.5  | < 6.4   | ...                              | ...                              | ...                               |
| TN J2007-1316  | WCD   | 4       | SB2         | 15.0   | 8.8± 1.7   | 6.2± 1.3  | 7.9                              | 0.70                             | 0.158                             |
| MRC 2025-218   | WD    | 2       | SB2         | < 3.1  | 1.6± 0.3   | < 6.3   | > 1.4                            | > 0.1                            | > 0.02                            |
| MRC 2048-272   | UL    | 0       | SB2         | < 4.7  | < 2.1  | < 3.2   | ...                              | ...                              | ...                               |
| MRC 2104-242   | WCD   | 5       | SB2         | 8.0  | 2.8± 1.0   | 5.2± 1.2  | 3.0                              | 0.27                             | 0.060                             |
| 4C 23.56*      | WD    | 5       | SB2         | < 23.7   | 24.5± 1.7  | < 5.4   | > 24.9                           | > 2.2                            | > 0.49                            |
| MG 2144+1928   | WCD   | 2       | SB2         | 12.3   | 8.5± 2.1   | 4.4± 0.9  | 11.0                             | 0.99                             | 0.221                             |
| USS 2202+128   | WD    | 4       | SB2         | < 10.0   | 7.3± 1.1   | < 4.2   | > 9.7                            | > 0.8                            | > 0.19                            |
| MRC 2224-273   | WCD   | 3       | SB1         | 3.4  | 1.9± 0.3   | 2.2± 0.7  | 3.3                              | 0.45                             | 0.092                             |
| B3 J2330+3927  | WCD   | 6       | SB4         | 24.5   | 13.6± 2.4  | 10.9± 0.9                                       | 4.5                              | 0.76                             | 0.096                             |
| 4C 28.58       | WCD   | 8       | SB6         | 17.7   | 8.1± 1.2   | 9.6± 1.0  | 4.5                              | 0.30                             | 0.096                             |
| 3C 470         | WCD   | 7       | SB1         | 8.8  | 3.8± 0.8   | 4.9± 0.6  | 3.2                              | 0.45                             | 0.092                             |

## Appendix A: Notes on sources

*B2 0902+34* (WCD with 3 detections): This object is the only radio galaxy from our sample to be most likely dominated by synchrotron emission (Archibald et al., 2001). We therefore treat this galaxy as if it were actually a member of the UL class for the purposes of fitting its SED.

*4C 23.56* (WD with 5 detections): This object is the prototypical case where the IR emission is dominated by the emission from the AGN. There are other pieces of evidence from other wavelengths to support this dominance. For instance, rest frame UV shows strong polarisation (Cimatti et al., 1998); the IRAC colors are characteristic of sources dominated by AGN emission in rest frame near-IR (Fig. De Breuck et al., 2010); X-ray emission is also prominent and suggestive of emission from an AGN. This radio source can be seen as having the most extreme AGN contribution to its SED in our sample. We stress that the Mullaney AGN template reproduces well the SED of *4C 23.56* without any modification. This indicates that the AGN DecomPIR template can be a good representation of AGN emission in our sample.

*4C 41.17* (WCD with 7 detections): Of course, with a radio galaxy dominated by its AGN in the infrared, it would be interesting to have the opposite, a radio galaxy dominated with its IR SED dominated by star formation. *4C 41.17* likely represents such a case. This radio source has a SB dominated SED, and can be reproduced well by the SB6 template. A more complete SED decomposition confirms this results (Rocca-Volmerange et al., 2013).

## Appendix B: AGN or SB dominated ?

We remind that  $f_{\text{AGN}}$  is defined as the ratio  $S_{\text{AGN}}/S_{\text{SB}}$  where  $S$  is the flux of the AGN and the SB respectively, at 10, 50 and  $100\mu\text{m}$ . Figure B.1 plots the  $f_{\text{AGN}}^{10,50,100\mu\text{m}}$  fraction as a function of the total infrared luminosity,  $L_{\text{tot}}^{\text{IR}}$  (see § 3.1). This fraction of AGN emission at 10, 50 and  $100\mu\text{m}$  allow us to check whether the emission at the probed wavelength is dominated by AGN emission or not.

The top plot shows that independently from the classification introduced in § 3.2, the AGN contributes *at least* to 50% of the flux at  $10\mu\text{m}$ . In contrast, at  $100\mu\text{m}$  (bottom plot), the AGN is generally at the  $\leq 10\%$  level. However, we can see that even at such long wavelengths, the contribution of the AGN can, from time to time, be exceptionally high (almost 50%). This latter could refer to extreme objects such as *4C 23.56* or to extended dust emission (Dicken et al., 2010). At  $50\mu\text{m}$  (middle plot), we can clearly see that AGN can be from dominant to completely negligible. We conclude that even trying to define classes to potentially differentiate between AGN and SB dominated objects from data is almost impossible for high redshift radio galaxies. Only a SED decomposition as presented in § 4 can finally settle this question.

## Appendix C: Bolometric correction

In order to derive AGN intrinsic properties, the AGN bolometric luminosity is needed. Hard X-rays provide the best approximation to the bolometric luminosity as most of the material along the line-of-sight is optically transparent. We do not possess X-rays measurement for our entire sample, we therefore make use

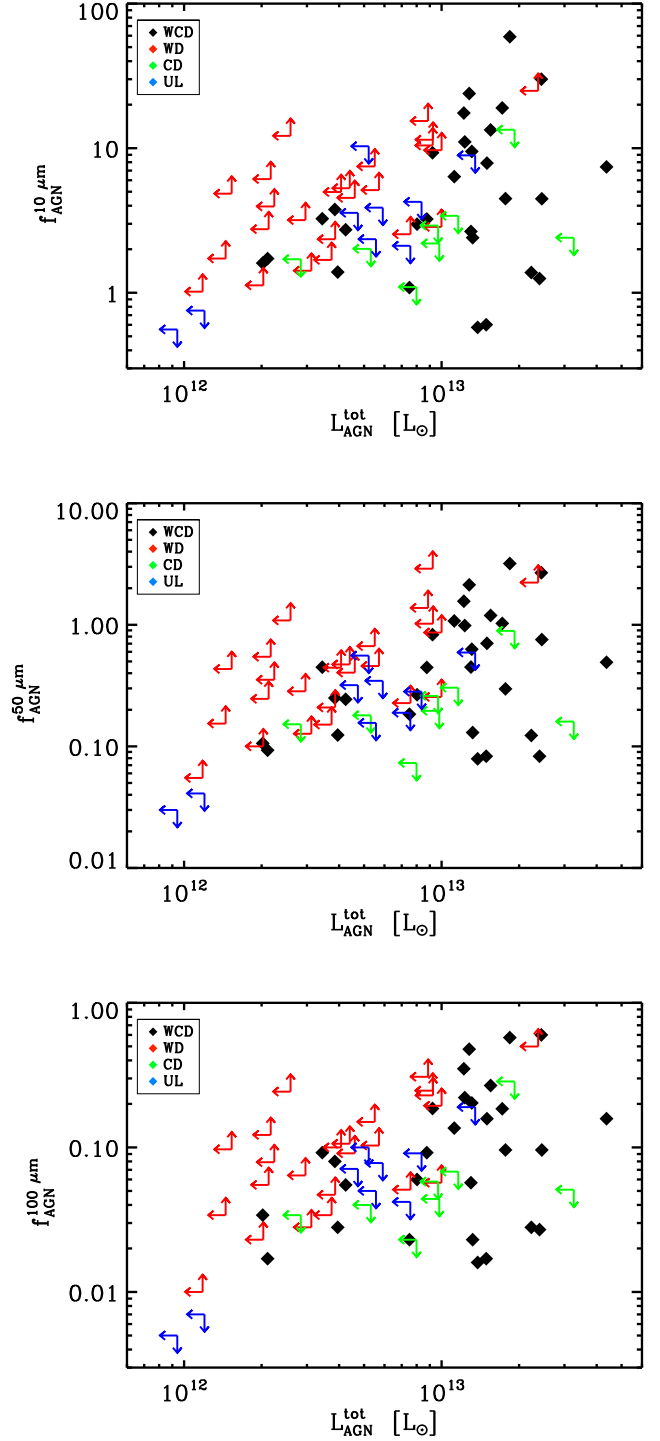


**Fig. B.1.** From top to bottom, AGN fraction at 10, 50 and  $100\mu\text{m}$  against the total infrared luminosity. The colour and symbols corresponds to the class defined in § 3.2

of the calculated infrared luminosities. Numerous attempts to derive bolometric correction factor have been done (e.g. Elvis et al., 1994; Haas et al., 2003; Marconi et al., 2004; Krawczyk et al., 2013; Hao et al., 2014; Scott & Stewart, 2014). Although essential, they are subject to significant variation from object to object. For our SED range Elvis et al. (1994); Richards et al. (2006) provide some correction factor depending on the



observed wavelength. This correction factor can be as small as 2 and as high as 20 for X-rays, depending mainly on the morphology. We here want an approximation of this factor for our sources.

First, we can use a purely geometrical approach. Assuming the torus around AGN to be optically thick at all wavelengths, it absorbs light from across the electromagnetic spectrum and re-radiates in IR. We can use the statistical distribution of type 1 and type 2 AGN in the sky (Barthel, 1989). The solid angle for an opening angle of  $45^\circ$  corresponds to a factor  $\sim 2$ . This is expected to be the minimum correction.

Second, we can assume that the nuclei in type 2 and type 1 AGN are similar. Using a type 1 radio loud AGN template from Elvis et al. (1994) and assuming that the total IR luminosity does not depend strongly on orientation, the bolometric correction factor is  $\sim 6$ . Doing the same exercise with the Richards et al. (2006) template gives a correction factor of  $\sim 5$ .

Third, some sources in our sample possess X-ray observations (Carilli et al., 2002). Integrating the energy over X-rays, it appears that X-rays does not present the most significant contribution to the bolometric luminosity.

As the radio emission is highly directional (i.e. subject to strong beaming effect), its inclusion in the bolometric factor is highly uncertain. Type 2 AGN SEDs show that the integrated radio energy is roughly at the X-ray level. Its contribution to the total energy should not be the most significant.

Estimation of the bolometric correction is rather difficult and uncertain. Nevertheless, the geometric approach and the moderate contribution from X-rays and radio indicates that most of the light comes from the UV-optical from the central AGN part and the reprocessed light by the dust. Therefore, a factor of 6 seems appropriate in the case of radio galaxies to convert  $L_{\text{AGN}}^{\text{IR}}$  to  $L_{\text{AGN}}^{\text{Bol}}$ .

## Appendix D: Summary of the global uncertainties

Since we are using various approximations throughout this paper which can have an impact on this analysis, we summarise here each of these and discuss their possible impact on our interpretation.

(i) The validity of the  $M_{\text{BH}}-M_{\text{Bulge}}$  relation at high redshift deserves some attention. The first part of this relation is to consider the estimated stellar mass as the mass of the bulge or spheroid of individual galaxies. *HST* observations have shown that radio galaxies have elliptical light profiles (van Breugel et al., 1998; Pentericci et al., 1999, 2001; Zirm et al., 2003). Nevertheless, these determinations represent the radially averaged or global best-fit light profile with moderate-to-low signal-to-noise and the possible presence and contribution from sub-structure and heavily obscured younger disk components cannot be excluded in the profile fitting (see Hatch et al., 2013). After all, our estimates of the star formation rates suggest that obscuration could be important and since the gas supporting such intense star formation would be highly dissipative and could easily be in a disk. However, the stellar masses estimated by De Breuck et al. (2010) are measured in the rest-frame *H* band, minimizing the impact of extinction and also sampling more appropriately the older population (modulo the contribution from young super-giants). The measured mass can therefore be considered as the total mass of the system and at least, in principle, sensitive to the older generations of stars in the host galaxy (Rocca-Volmerange et al., 2013). Considering the  $M_{\text{BH}}-M_{\text{Bulge}}$  relation itself, Jahnke et al. (2009) estimate that the  $M_{\text{BH}}-M_{\text{stel}}$  relation shows little variation from  $z=1.4$  to  $z=0$ .

(ii) The radiative efficiency of the accretion,  $\epsilon$ , is not well-constrained and is certainly not a constant. This factor can vary from 0.06 to 0.42, related to the spin of the black hole (Krolik, 1999). There are attempts to constrain the spin of radio loud AGN in the literature. Martínez-Sansigre & Rawlings (2011) show that black hole spins tend to be lower at higher redshift even with the presence of a bimodal distribution. As these constraints are quite poor at high redshift, it is impossible to conclude on the possible value of  $\epsilon$ , but perhaps a range of a few is reasonable (factor 3 at maximum).

(iii) The correction factor to estimate the bolometric luminosity,  $\kappa_{\text{AGN}}^{\text{Bol}}$ , shows a wide variety of possible values. Pure geometric considerations imply that  $\kappa_{\text{AGN}}^{\text{Bol}} > 1.4$  and is unlikely to be  $> 10$  for the conversion of IR luminosity to bolometric luminosity (see Appendix A for details). We assumed  $\kappa_{\text{AGN}}^{\text{Bol}} = 6$  for the ensemble of radio galaxies. This correction is not expected to differ strongly from this value as the energy is mostly radiated in IR in our object and we have now a good coverage of this part of the SED. However, a factor as low as 2 is not unreasonable (see Appendix C).

(iv) The sSFR calculated are dependant on the canonical law used to transform  $L_{\text{SB}}^{\text{IR}}$  into SFR and the stellar mass. While the Kennicutt (1998) relation seems to represent well most star forming galaxies, some discrepancies are expected as it is dependent of the star formation law. Indeed, Calzetti (2012) lists the impact of the approximation on the different SFR indicators at various wavelength. This also depends on  $\tau$  and the adopted IMF; the variation can be a factor of a few (up to  $\sim 6$ ). Also, the IMF can induce a factor of  $\sim 2$  in the stellar masses estimates (e.g. Marchesini et al., 2009). This effect will move the points horizontally in Figure 9.

(v) The AGN SED can present a wide variation (e.g. Nenkova et al., 2008; Fritz et al., 2006). As mentioned, our generic AGN SED can miss a part of the extended flux from the AGN heating of the NLR (e.g. Dicken et al., 2009; Pier & Krolik, 1993). However, as we are dealing with integrated luminosities over the 8-1000  $\mu\text{m}$  range, the calculated  $L_{\text{AGN}}^{\text{IR}}$  is expected to differ strongly only with a drastic change of the AGN SED which is unlikely (§ 4.2). The most probable case would be that we underestimated the AGN contribution, therefore, all corresponding values will be increased by the same factor, increasing the offset from the local  $M_{\text{BH}}-M_{\text{Bulge}}$  relation.

## SEDs

**Fig. D.1.** SEDs of the 70 radiogalaxies sorted by RA. IRS and MIPS data taken from De Breuck et al. (2010), PACS and SPIRE data in Table 3 and sub-mm data in Table 4. Filled diamonds, the firm detections ( $>3\sigma$ ), open diamonds the weak detections ( $2\sigma < F^{\text{gal}} < 3\sigma$ ) and downward triangles the  $3\sigma$  upper limits. The red downward triangles mark to the most constraining upper limit. Continuous line represents for fitted components, depending on the class: AGN for WD, SB for CD and sum of AGN and SB for WCD (as marked in the figure legend). The 6 stamps correspond to the MIPS ( $24\ \mu\text{m}$ ) and the five *Herschel* observations when available, with north at the top, east at the left, centred on the radio coordinates of the radio galaxy. Each stamp covers  $2 \times 2$  arcmin. We also overplot the IRS spectra when available for the source (Seymour et al., 2008; Rawlings et al., 2013).

